Highlights

An experimental investigation into smoothly nonlinear rotordynamics

Mehmet Selim Akay, Alexander D. Shaw, Michael I. Friswell

- First experimental demonstration of cubic geometric nonlinearity exciting internal resonances.
- Observed 2:1/3:1 internal resonances, precession switching, and mode-locked behaviours.
- Geometric nonlinearity alone can generate dangerous internal resonances.
- Developed a versatile experimental platform for rotordynamics research.

An experimental investigation into smoothly nonlinear rotordynamics

Mehmet Selim Akay[a], Alexander D. Shaw[a] and Michael I. Friswell[a]

[a]Swansea University, Bay Campus, Swansea, SA1 8EN, Wales, UK

ARTICLE INFO

Keywords:
Nonlinear rotordynamics
Internal resonance
Geometric nonlinearity
Rotor-stator interaction
Experimental investigation

ABSTRACT

Nonlinear rotor-stator interactions in rotating machinery can lead to dangerous internal resonances (IRs) that threaten structural integrity. While contact-based nonlinearities (friction, impact) have been extensively studied experimentally, geometric nonlinearities—which can excite similar IR modes at lower amplitude levels—have received limited experimental validation. This paper presents experimental investigations of nonlinear rotor-stator bouncing interactions using a purpose-built test rig featuring cubic geometric nonlinearity generated through bend-stretch coupling. The test rig comprises a cantilever rotor with an overhung disk to induce prominent gyroscopic effects, coupled to a stator through pinned-pinned rods that create cubic stiffness. A four-degree-of-freedom mathematical model is developed to predict the system's nonlinear response and generate bifurcation diagrams for comparison with experiments. Modal testing characterises the linear dynamic properties, while run-up and coast-down experiments across varying speeds and unbalance levels reveal complex nonlinear phenomena. The experiments successfully demonstrate the excitation of theoretically predicted internal resonances, including 2:1 and 3:1 responses, forward-to-backward precession switching, and mode-locked behaviours. Key findings include the observation of backward resonance, orbit stagnation at precession direction transitions, and "parked" orientations due to support anisotropy. The results validate that cubic geometric nonlinearity alone can generate dangerous IR responses, providing new insights into nonlinear resonance mechanisms in rotating machinery and establishing a versatile experimental platform for future rotordynamics research.

1. Introduction

Nonlinear rotor-stator interactions are critical phenomena in rotating machinery, particularly in turbomachinery and drilling applications where small clearances and high operational demands can lead to complex dynamic behaviours [1]. Pioneering studies such as by Ehrich [2] and Black [3] revealed that rotor-stator contact could produce a remarkably diverse range of dynamic behaviours depending on system parameters such as friction coefficients, clearances, stiffness ratios, and excitation levels. Theoretical observations of the rub-impact phenomena have been documented in numerous publications over recent decades [4, 5, 1]. However, experimental observations are relatively less commonly published due to the dangerous and difficult nature of such experiments [6].

1.1. Nonlinear responses

Synchronous and asynchronous, periodic, quasiperiodic, and chaotic responses have been observed both theoretically and experimentally. Experimental literature documents full rubbing phenomena relatively comprehensively [7, 8, 9, 10, 11], though theoretical research to understand the mechanisms continues [12].

Various forms of intermittent-contact or bouncing responses have been studied. The subharmonic response was commonly encountered in unbalance response involving rub-impact [13, 14, 15, 14, 16, 17], though Torkhani et al. [6] did not observe subharmonic responses in a real-scale test rig. The super-sub harmonic resonance of order 2/5 was seen in the experiments of Ishida et al. [15]. The subharmonic response was expected in other studies [18, 16] in the presence of contact and anisotropy.

The Zilli system and internal resonances (IRs) A particularly important development in the theoretical understanding of bouncing limit cycles came after Zilli et al. [19], who investigated a 2-dof, snubbed overhung rotor with

*Corresponding author
m.s.akay.856478@swansea.ac.uk (M.S. Akay); a.d.shaw@swansea.ac.uk (A.D. Shaw); m.i.friswell@swansea.ac.uk (M.I. Friswell)
ORCID(s): 0009-0009-4659-8961 (M.S. Akay); 0000-0002-7521-827X (A.D. Shaw); 0000-0003-4677-7395 (M.I. Friswell)

gyroscopic effects (the *Zilli system*), defining a synchronisation condition for locked frequencies. Shaw et al. [20] viewed the response as IR of any two whirl modes. These responses form when the vibration frequencies appear commensurate in the rotating frame (more in the following) [20, 18], while the underlying nonlinear modes exhibit mode-locked behaviour. Bouncing cycles in the form of IRs represent particularly important nonlinear phenomena that have received increasing attention [19, 21, 22, 23, 24, 25]. Very recently, Shaw et al. [26] have introduced a novel backbone method to understand the formation of these IR modes through constraining the response of underlying conservative isotropic rotor system.

The IR responses of order p:q in the stationary frame has the frequency relation,

$$p\omega_f^{sta} - q\omega_b^{sta} = (p-q)\Omega \tag{1}$$

where $\omega_f^{sta} > 0$ and $\omega_b^{sta} < 0$ are the forward (FW) and backward (BW) underlying whirl velocities of the IR mode in the stationary frame – main contributors to the IR mode along with the rotor speed Ω due to out-of-balance forcing; p and q are integers. The relation in the rotating frame becomes,

$$p\omega_f^{rot} = q\omega_b^{rot} \tag{2}$$

where $\omega_f^{rot} = \omega_f^{sta} - \Omega$ and $\omega_b^{rot} = \omega_b^{sta} - \Omega$ are the FW and BW underlying whirl velocities in the rotating frame, while the drive speed Ω disappears in the rotating frame, creating the IR frequency relation. Optionally, the notation p^a:q^b with a and b positive integers, can be used to refer to the a^{th} and b^{th} FW-BW pair of modes. The 2:1 IR response has been predicted theoretically, particularly in systems with prominent gyroscopic effects [15, 27], but less frequently documented experimentally. Yoshimori et al. [25] studied the effect of stator thickness, observing IRs of orders 2:1 and 3:1. Wang et al. [23] investigated how contact stiffness changes alter IR response, observing richer IR responses including 7:1 and 5:1 resonances in addition to the more common 2:1 and 3:1 modes, but only with high contact stiffness. Experimentally, Crespo et al. [28] observed 2:1 response in a narrow range of rotor speeds on a multi-dof rotor system. Due to small basin of attraction [29], 3:1 IRs are even more seldom observed. It appears that IR response is not achieved in the experiments as full branch of solutions but partially. The present work aims to understand this kind of IR response in a more comprehensive way by drawing a complete branch of 2:1 IRs.

Rotating frame perspective An essential conceptual advance in understanding rotor-stator interactions has been the recognition that many nonlinear responses exhibit periodicity in the rotating rather than stationary frame of reference. This is a coordinate frame rotating about the constant shaft axis with rotor spin speed, hence also called the co-rotating frame. The physical explanation is that in the rotating frame, the out-of-balance forcing appears as a static force at the DC component of the frequency spectrum while the modal frequencies become commensurate. Quasiperiodic responses which appear periodic in the rotating frame are characteristic of rotating IR modes [18]. Shaw et al. [20] defined the IR phenomenon explicitly in the rotating frame and generalized the concept to multi-dof models. In a subsequent work [21], they used the rotating frame and signed Campbell diagrams to conveniently locate the branch onset of IR motion along the rotor speed range. Recent studies [23, 25] have further stressed the rotating coordinate system's importance for revealing periodic bouncing cycle responses. Cole and Keogh [30] emphasised rotating frame periodicity on a friction related response, though not an IR, which is also observed in the present study.

1.2. Test rigs

Test rig scale and purpose Depending on research aims, test rig scale varies considerably. For high-fidelity representation of real-scale turboengines, large test rigs are employed [13, 6, 31], while for isolation of specific nonlinear phenomena, smaller versatile bench-top scale rigs are preferred [32, 7, 8, 14, 33, 9, 34, 35, 15, 36, 37, 31, 17, 38]. A close investigation of IR responses can better be managed with a dedicated smaller-scale model in a more controlled manner.

Test rig versatility Building a versatile rig ensures richer investigations of nonlinear rotordynamics. Test rigs that aim versatility include the Bently Nevada test rig [39] which was used in [33, 7, 40], and TUD rig in [41]. A dual rotor speed ratio was variable in [38]. Refs. [6, 24] varied contact surfaces to alter friction. Clearance adjustment methods vary: changing stators [42, 14, 43], or using conical systems [44, 17]. Chipato et al. [22] adjusted stator stiffness by changing rod lengths. Because generally the stator is the source of nonlinearity, the present paper employs a rig that allows for different stator designs.

Rotor configurations Numerous rotor configurations have been employed in experimental research. Multi-disk rotors featured in [14], while dual-rotor configurations appeared in [45, 38, 46]. Slender shafts with bend-stretch coupling were investigated in [37, 35]. Ishida et al. [15] investigated a 4-dof extended Jeffcott rotor with contact. Overhung rotors with contact appeared in [32, 36, 23]. Disk rotation achieved in some way enables generality with gyroscopic effects included.

For assuring a smooth drive, flywheels can isolate the rotor, as in [37, 8]. Choi [8] used flexible coupling, flywheel, and belt driver to keep measured rotor vibration clean of drive frequencies. However, in many rotors with disks, the rotor itself can provide sufficient rotational inertia to smooth slightly non-ideal motor drive. Despite using soft plastic pipes for rotor-motor isolation, Nagasaka et al. [37] reported no unstable internal damping. Prevention of internal damping through micro-slip at connecting interfaces was assured by high clamping force in the conical shaft attachments in the TUD rotor test rig [41]. Though, avoidance of internal resonance is preferable to isolate the nonlinear phenomena at target.

Physical effects Gravity effects have been commonly included [17, 43], which produced multi-periodic and chaotic responses [47]. Though, increased rotor stiffness [47] or rotor speed [48] nullified these gravity effects. Saeed et al. [49] employed a coordinate transformation to eliminate the gravity term from equations of motion, resulting in quadratic position terms. Shaft asymmetry was investigated under gravity loads on slender shafts [37]. Torsional vibrations [34], preloaded stiffness [42], earthquake-like excitation [9] and shaft bow [43, 6] were studied in experiments. Transient motion during run-up or run-down under unbalance excitation was studied in [7, 6], and upon sudden unbalance in [31]. Gyroscopic effects were seen in [32] on an overhung disk. The extended Jeffcott rotor (off-centre disk) provided gyroscopic effects in [15]. However, vertical rotors can generally ignore gravity without hindering the calculations accuracy [47].

Nonlinearity sources Nonlinearity arose from bend-stretch coupling in [37, 35, 50] due to axial constraint on elastic shaft elongation. Other studies employed annular rings [22, 6, 31, 15], creating nonlinearity through discontinuous stiffness. Partial rub devices [13, 16, 33], or unconventionally, a pinned snubber [36], an inner stator contact [9] and a piecewise linearly achieved continuous cubic stiffness [51] have appeared. However, unconventional methods are not preferred if the nature of common response types are to be analysed.

Different contact models and cubic stiffness The contact models range from rigid impact laws [30, 52] to compliant stiffness definitions with piecewise-linear functions [53]. Wang et al. [23] systematically studied effects of contact stiffness. Shaw et al. [20] investigated stators with stiffnesses of 0.1 MN/m and 10 MN/m. Similar backward resonances were observed in rigid impact [30] and soft contact [54]. Wide range of stiffness ratios investigated across the literature suggests that smooth nonlinearities could generate similar responses to discontinuous stiffness models of rotor-stator interaction. This observation motivates the present study's focus on geometric nonlinearity as a fundamental mechanism capable of producing dangerous IRs without requiring physical contact.

1.3. Research gap and motivation

Despite significant progress in both theoretical and experimental rotordynamics research, several important gaps remain. While contact-based nonlinearities (friction, impact, compliant stiffness) have been extensively studied, geometric nonlinearities have received less experimental attention despite theoretical predictions that they can generate similar IR responses at lower amplitude levels. Particularly, the experimental research is sparse that focuses on the 2:1 and 3:1 IRs and their associated mode-locking behaviours. The evolution of these responses with rotor speed is not investigated previously, which might create new tools for condition monitoring. For researching different nonlinearities, stator versatility needs to be improved.

The present study addresses these gaps by designing and implementing a bench-top test rig featuring cubic geometric nonlinearity generated through bend-stretch coupling, with an overhung disk configuration to induce prominent gyroscopic effects presenting a unique tool for rotordynamics research, particularly for IR responses.

The remainder of this paper is organised as follows: Section 2 describes the test rig design and instrumentation. Section 3 describes the development of a 4-dof mathematical model. Section 4 gives the experimental calibration and quantification such as measuring the shaft bend, natural frequencies, and force-displacement curves. Section 5 presents the results in terms of bifurcation diagrams (BDs) and compares experimental findings with theoretical predictions, discussing agreements, discrepancies, and physical mechanisms. Section 6 draws conclusions and suggests directions for future research.

2. Design of the test rig

2.1. General description

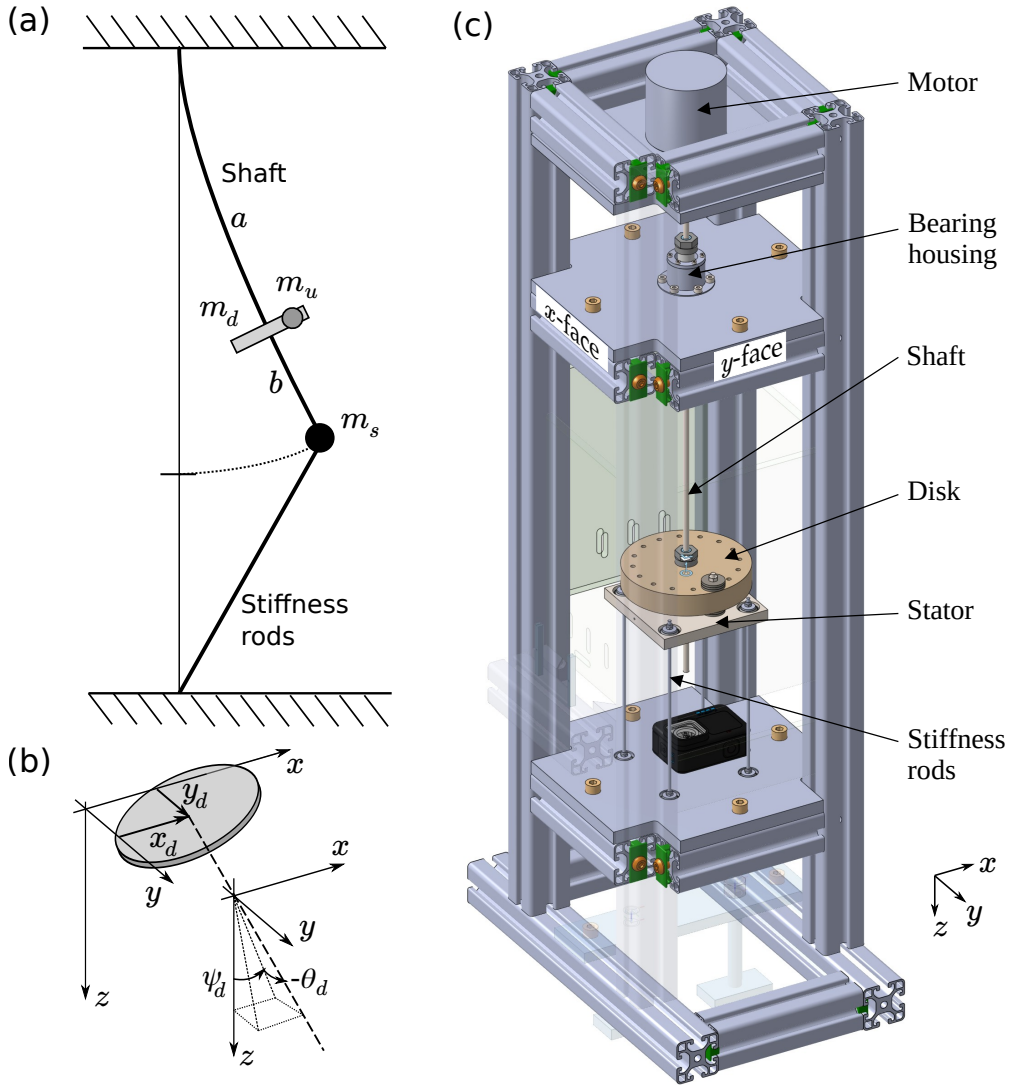

Figure 1: (a) Schematic of the equilibrium when the stator is displaced. (b) Schematic for the small disk angles. (c) 3D global assembly drawing of the test rig. Main parts, coordinate frame and x- and y-faces are indicated. Protective polycarbonate sheets, one pillar of the frame and sensor attachments kits are rendered transparent for a clearer view. Shims that are used to centre each level with respect to the frame are not shown.

The 3D drawing of the rig is given in Figure 1. It has a steel cantilever shaft that is connected to the disk towards the free tip where the shaft may be coupled to the stator.

The shaft is driven by a BLDC58-50L electric motor, which features integrated speed control, located at the top plate. The bearing housing is located under the motor plate, where a pack of three angular contact ball bearings in DBD configuration satisfy cantilever boundary conditions for the upper shaft support.

In order to be comparable in dynamics to the preceding theoretical studies in [29, 55] which were inspired by Zilli et al. [19], a 2-dof cantilever model was derived in [56] which will be omitted here for brevity. This 2-dof system was also used to create an initial estimate for the damping for simulations. However, due to the high number of connecting joints, the damping is bound to be difficult to measure. Therefore, the experimental results were used to update the damping value. Estimated bearing forces for the selection of bearings were also calculated [56]. In order to create a

test rig in bench-top sizes, an initial decision of 5 mm shaft diameter was made. Then, stiffness and mass values as well as other dimensions (see Section 5.2.1) were selected so that the natural frequencies, unbalance excitation levels and the cubic stiffness are comparable to the preceding theoretical studies [29, 55].

2.1.1. Nonlinear stiffness

The nonlinear stator stiffness is achieved with stiffness rods connected to the stator similar to [8, 42, 22]. However, here the rods are connected to the ground with pinned-pinned boundary conditions, creating a bend-stretch coupling when the stator reaches significant vibration amplitude. This system is similar to a spring whose one end is fixed and the other is displaced laterally (see schematic in Table 1). Taylor expansion of the lateral component of the tension force in the spring, $F_y = ky\left(1 - l/\sqrt{y^2 + l^2}\right)$, is given in Table 1 which is utilised to plot Figure 2. Figure 2 shows that the dominant contribution for the axial lateral force is cubic, and the error is below 1% up to a lateral displacement ratio of 0.1. This shows that the lateral force generated by a bend-stretch coupling in a cantilever-pinned-pinned system will be close to a purely cubic force just as it was used in the preceding theoretical works [29, 55]. Experimental force-displacement curves later will confirm that (Figure 9).

Table 1
Taylor expansion for the lateral force, $F_y = ky\left(1 - l/\sqrt{y^2 + l^2}\right)$, for a spring that elongates under lateral tip motion while the other end is fixed.

Schematic	Number of terms	Taylor expansion ($\bar{y} = y/l$)
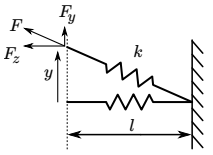	1,2,3	0
	4,5	$k\bar{y}^3/2$
	6,7	$k\bar{y}(-3\bar{y}^4 + 4\bar{y}^2)/8$
	8,9	$k\bar{y}(5\bar{y}^6 - 6\bar{y}^4 + 8\bar{y}^2)/16$
	10,11	$k\bar{y}(-35\bar{y}^8 + 40\bar{y}^6 - 48\bar{y}^4 + 64\bar{y}^2)/128$

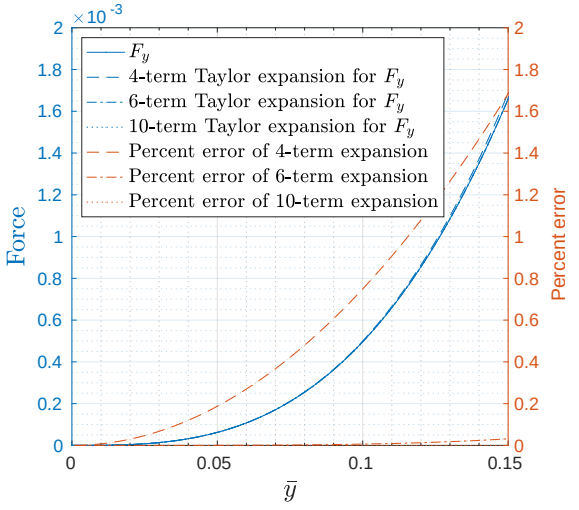

Figure 2: Lateral force F_y and its Taylor expansion for a spring that elongates with lateral tip motion while the other end is fixed. Here $\bar{y} = y/l$ is the ratio of lateral displacement to spring initial length.

2.2. Instrumentation

Data is acquired via a NI cDAQ-9178 chassis, using an NI-9223 module to receive signals and an NI 9263 module to provide a voltage signal that controlled the motor speed. In most test runs the sample rate used was 10 kHz if not otherwise indicated, chosen to be at least 100 times greater than the highest frequency of interest. The motor speed was verified by the signal from the motors' built in tachometer, which provided a voltage spike 36 times per revolution.

Two NI 252C03 piezoelectric accelerometers along with a PCB Piezoelectronics impact hammer were used for tapping tests, all with ICP current of 4 mA.

3. Mathematical model

This section defines a 4-dof model of the experimental rig. The shaft mass is neglected, although some additional equivalent mass is included in the disk. The axial stator to disk distance is assumed to be short enough to approximate a rigid connection between them. Axial and torsional dynamic effects are neglected because the natural frequencies of these motions are expected to be much higher than the lateral frequencies. The generalised coordinates are the lateral translational displacement pair and angular displacement pair of the disk (Figure 1b).

The energies of the 4-dof system and the Lagrangian function can be expressed as follows,

$$T_{tra} = \frac{1}{2}m_d\left(x_d'^2 + y_d'^2\right) + \frac{1}{2}m_u\left(x_u'^2 + y_u'^2\right) + \frac{1}{2}m_s\left(x_s'^2 + y_s'^2\right) \tag{3}$$

$$T_{rot} = \frac{1}{2}J_d\left(\theta_d'^2 + \psi_d'^2\right) + \frac{1}{2}J_p\left(\Omega^2 - 2\,\Omega\psi_d'\sin\theta_d + \psi_d'^2\sin^2\theta_d\right) \tag{4}$$

$$T_{tot} = T_{tra} + T_{rot} \tag{5}$$

$$V_{tot} = \frac{1}{2}\mathbf{w}_{elastic}^T\mathbf{K}\mathbf{w}_{elastic} + \frac{1}{2}k_{rb}r_s^2 + \frac{1}{4}k_{3b}r_s^4 \tag{6}$$

$$L = T_{tot} - V_{tot} \tag{7}$$

$$\delta W_{nc}^{active} = -x_s'c_{rb}\delta x_s - y_s'c_{rb}\delta y_s \tag{8}$$

where T_{tra}, T_{rot} and T_{tot} are the translational, rotational and total kinetic energies, V_{tot} is the total strain energy, L is the Lagrangian function. Here, m_d, m_u and m_s are the disk mass, the unbalance mass attached to the disk with an eccentricity, and the stator mass. x_d, x_u and x_s are the disk, unbalance and stator's x-axis positions, with y-axis counterparts. The stator's lateral position amplitude is denoted $r_s = \sqrt{x_s^2 + y_s^2}$. Cantilever shaft stiffness matrix is $\mathbf{K}$ while k_3b is the radial cubic stiffness acting at the stator, and c_{rb} is linear radial damping at the stator. δW_{nc}^{active} is the nonconservative active forces' virtual work. The textbook [57] explains further the rotational kinetic energy of a disk. The generalised coordinates are,

$$\mathbf{w} = \{x_d,\ y_d,\ \theta_d,\ \psi_d\}^T = \mathbf{w}_{elastic} + \mathbf{w}_{bend}, \tag{9}$$

where the total deflection is the result of the elastic displacement $\mathbf{w}_{elastic}$ and the bend displacement at the disk $\mathbf{w}_{bend}$ which is given by,

$$\mathbf{w}_{bend} = \mathrm{Re}\left(\begin{Bmatrix} \varepsilon_b\exp(j\delta_b) \\ -j\varepsilon_b\exp(j\delta_b) \\ j\beta_b\exp(j\gamma_b) \\ \beta_b\exp(j\gamma_b) \end{Bmatrix}\right) \tag{10}$$

which will be measured on the rig and given later below. The stator displacements are,

$$x_s = x_d + \psi_d b \tag{11}$$

$$y_s = y_d - \theta_d b \tag{12}$$

$$r_s^2 = x_s^2 + y_s^2 = x_d^2 + y_d^2 + \left(\theta_d^2 + \psi_d^2\right)b + 2x_d\psi_d b - 2y_d\theta_d b, \tag{13}$$

where b is the distance from the disk to stator. The unbalance displacements are,

$$x_u = x_d + \varepsilon_u\cos\phi \tag{14}$$

$$y_u = y_d + \varepsilon_u\sin\phi \tag{15}$$

$$x_u' = x_d' - \varepsilon_u\Omega\sin\phi \tag{16}$$

$$y_u' = y_d' + \varepsilon_u\Omega\cos\phi \tag{17}$$

where ε_u is the unbalance eccentricity, and unbalance moment is neglected. The shaft stiffness matrix is,

$$K = \begin{bmatrix} k_{uu} & 0 & 0 & k_{u\psi} \\ 0 & k_{vv} & k_{v\theta} & 0 \\ 0 & k_{v\theta} & k_{\theta\theta} & 0 \\ k_{u\psi} & 0 & 0 & k_{\psi\psi} \end{bmatrix} = \frac{2E_1 I_1}{a} \begin{bmatrix} 6/a^2 & 0 & 0 & -3/a \\ 0 & 6/a^2 & 3/a & 0 \\ 0 & 3/a & 2 & 0 \\ -3/a & 0 & 0 & 2 \end{bmatrix} \tag{18}$$

where E_1 and I_1 are the elastic modulus and 2nd moment of area of the shaft, a is the disk's distance from the cantilever root, and the **K** contains the stiffness coefficients for a clamped-free beam (as in the case of overhung rotor here) [57]. This essentially is an approximate model assuming a cubic displacement profile for the stator.

The 2nd type Lagrange's equations can be expressed as,

$$\frac{\mathrm{d}}{\mathrm{d}t}\left(\frac{\partial L}{\partial q_k'}\right) - \frac{\partial L}{\partial q_k} = Q_k\,, \quad Q_k = \frac{\partial \delta W_{nc}^{active}}{\partial q_k} \tag{19}$$

where q_k and Q_k are the k$^{\text{th}}$ generalised coordinate of **w** and k$^{\text{th}}$ generalised force linked to k$^{\text{th}}$ generalised coordinate. Then, the equation of motion is obtained,

$$\mathbf{M}\mathbf{w}'' + \mathbf{G}(\Omega)\mathbf{w}' + \mathbf{C}\mathbf{w}' + \mathbf{K}\mathbf{w} + \mathbf{N}(\mathbf{w})\mathbf{w} = \mathbf{b}$$

$$\mathbf{M} = \begin{bmatrix} m_d + m_u & 0 & 0 & 0 \\ 0 & m_d + m_u & 0 & 0 \\ 0 & 0 & J_d & 0 \\ 0 & 0 & 0 & J_d \end{bmatrix} + m_s\mathbf{P}\,, \quad \mathbf{G} = \begin{bmatrix} 0 & 0 & 0 & 0 \\ 0 & 0 & 0 & 0 \\ 0 & 0 & 0 & J_p\Omega \\ 0 & 0 & -J_p\Omega & 0 \end{bmatrix}$$

$$\mathbf{K} = \begin{bmatrix} k_{uu} & 0 & 0 & k_{u\psi} \\ 0 & k_{vv} & k_{v\theta} & 0 \\ 0 & k_{v\theta} & k_{\theta\theta} & 0 \\ k_{u\psi} & 0 & 0 & k_{\psi\psi} \end{bmatrix} = \frac{2EI}{a} \begin{bmatrix} 6/a^2 & 0 & 0 & -3/a \\ 0 & 6/a^2 & 3/a & 0 \\ 0 & 3/a & 2 & 0 \\ -3/a & 0 & 0 & 2 \end{bmatrix}$$

$$\mathbf{C} = c_{rb}\mathbf{P}\,, \quad \mathbf{N} = k_{3b}r_s^2\mathbf{P}\,,$$

$$\mathbf{b}_u = \Omega^2 \begin{Bmatrix} m_u\varepsilon_u\cos(\Omega t + \delta_u) \\ m_u\varepsilon_u\sin(\Omega t + \delta_u) \\ -(J_d - J_p)\beta_u\sin(\Omega t + \gamma_u) \\ (J_d - J_p)\beta_u\cos(\Omega t + \gamma_u) \end{Bmatrix}, \; \mathbf{b}_b = \mathbf{K} \begin{Bmatrix} \varepsilon_b\cos(\Omega t + \delta_b) \\ \varepsilon_b\sin(\Omega t + \delta_b) \\ -\beta_b\sin(\Omega t + \gamma_b) \\ \beta_b\cos(\Omega t + \gamma_b) \end{Bmatrix}$$

$$\mathbf{w} = \begin{Bmatrix} x_d \\ y_d \\ \theta_d \\ \psi_d \end{Bmatrix}, \quad \mathbf{P} = \begin{bmatrix} 1 & 0 & 0 & b \\ 0 & 1 & -b & 0 \\ 0 & -b & b^2 & 0 \\ b & 0 & 0 & b^2 \end{bmatrix}, \quad \mathbf{b} = \mathbf{b}_u + \mathbf{b}_b. \tag{20a}$$

In the experiments, the orientation of the shaft bow was aligned with the unbalance mass, and the shaft was assumed to be straight but only bent at the cantilever end as shown in Figure 3.

4. Experimental calibration

The experimental setup photograph is given in Figure 4. Several aspects of experimental calibration are presented below.

4.1. Characterising shaft bow and misalignment

In order to measure the shaft bow, the rotor is first run at very low speed (2.3 rad/s), which gives the inner circle in Figure 5, where the radius is used to infer that the amount of static deflection already present due to curvature of the shaft is 0.24 mm. Then it is run at a higher speed (170 rad/s), which gives the outer circle in Figure 5. This circle will include some influence from the out of balance forcing, and, therefore, will be more closely centred on the centre of rotation rather than the initial static position. Therefore, the difference between centres implies a small misalignment between the upper shaft support and the stator centre, which was seen to vary on each test run but remained small enough to neglect.

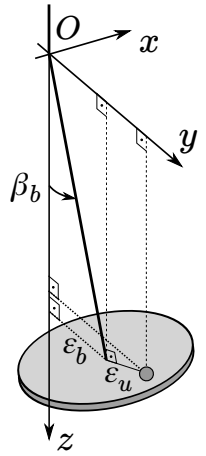

Figure 3: Schematic for showing the bend of the shaft and its alignment with unbalance mass orientation. The shaft is straight in the underformed form but only bent at the cantilever end. Both the unbalance mass and the bend are show in the yz-plane.

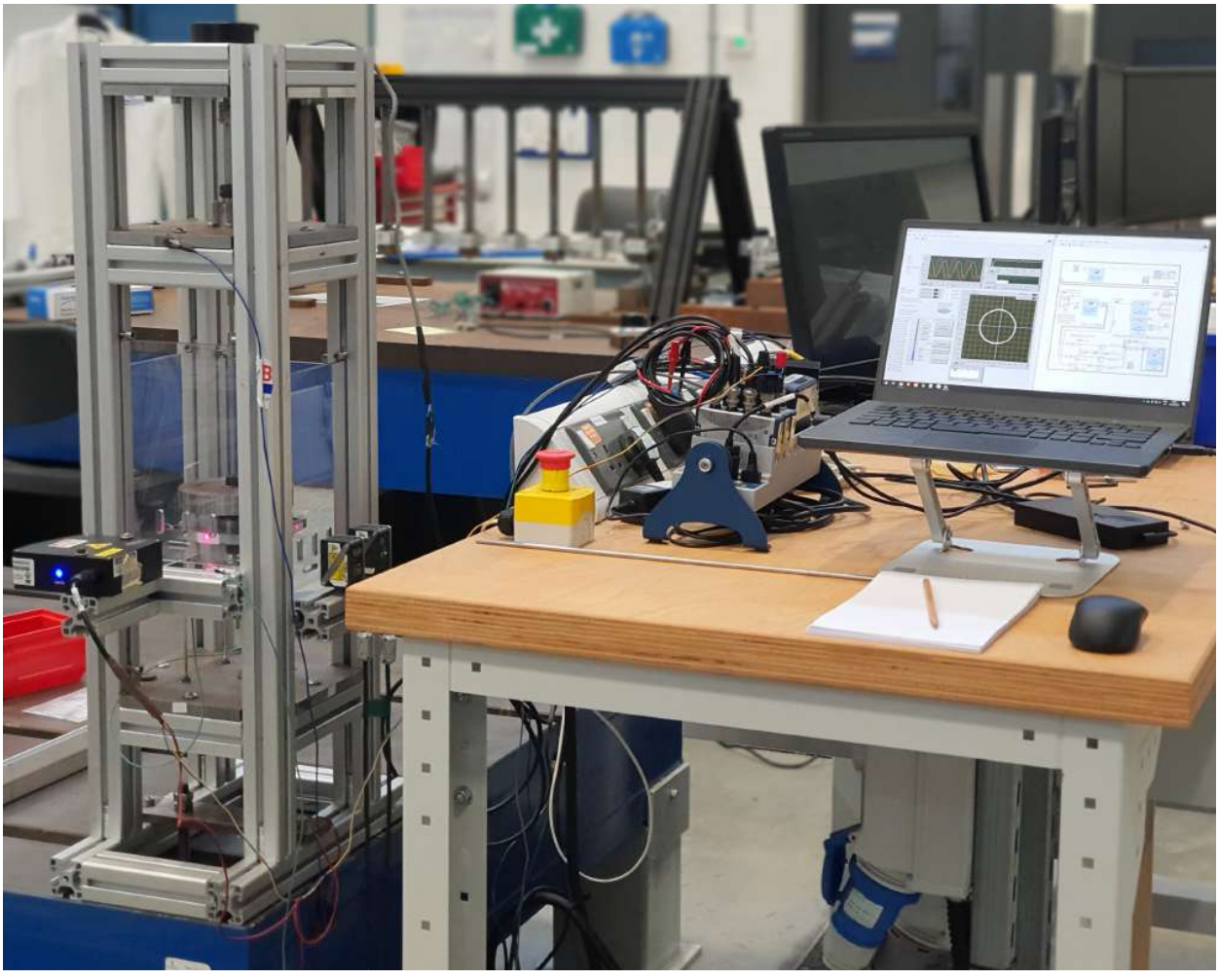

Figure 4: Photograph of the experimental test rig and data acquisition system.

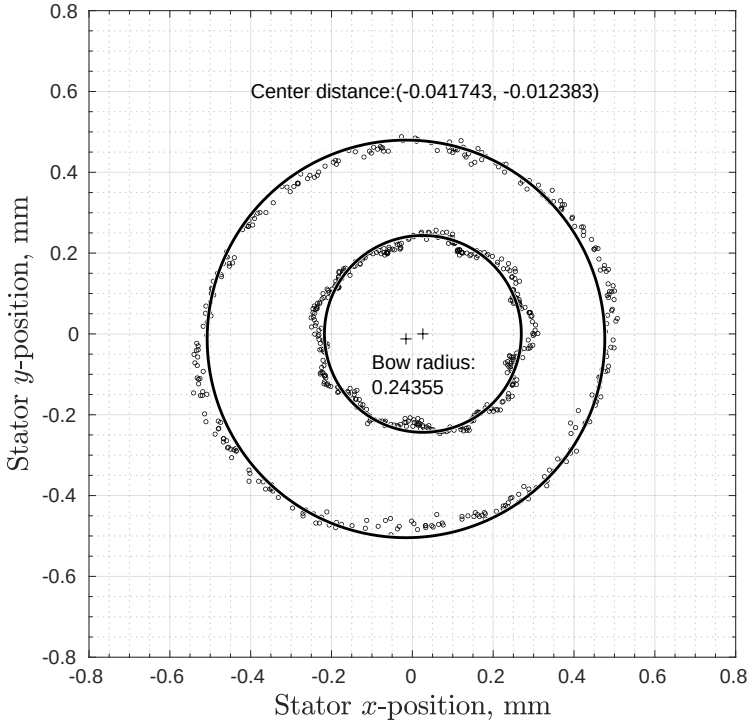

Figure 5: Shaft bend measurement – low (inner circle) and high speed (outer circle) runs' stator position samplings. Circles are compared.

4.2. Linear frequency tests

The rotor's Campbell plot was obtained by modal tap tests performed with the rotor spinning at various speeds. The impact location was the side of the stator on x-face and the accelerometer was fixed to the opposite side of the stator. The data was produced from 5 samplings of 5 sec duration each, at 25.6 kHz sampling rate. The results are given in Figure 6 with circles. The experimental impact test has a relatively consistent evolution with the rotor speed. The stiffness rods were left slack so that the underlying linear system is the dominant source of the results. The results are given in Figure 6. The measured Campbell plot matches the numerical one which utilises the values in Eq. (21) also used in the numerical simulations. The drive speeds where the linear frequencies satisfy the IR condition in Eq. (2) might be expected as tabulated in Table 2 from Figure 6.

Table 2
Expected internal resonances from the Campbell diagram in Figure 6.

Resonance	Expected rotor speed
$2^1{:}1^1$	$\Omega = 61.0$ rad/s
$3^1{:}1^1$	$\Omega = 40.7$ rad/s
$3^1{:}2^1$	$\Omega = 101.7$ rad/s
$2^1{:}1^2$	$\Omega = 206.0$ rad/s
$3^1{:}1^2$	$\Omega = 124.2$ rad/s

The test rig was seen to show some sensitivity to environmental factors such as temperature; therefore, further tap tests were conducted at the start and end of nonlinear test sessions. The observed frequencies were used to ensure that the properties of the system had not changed significantly.

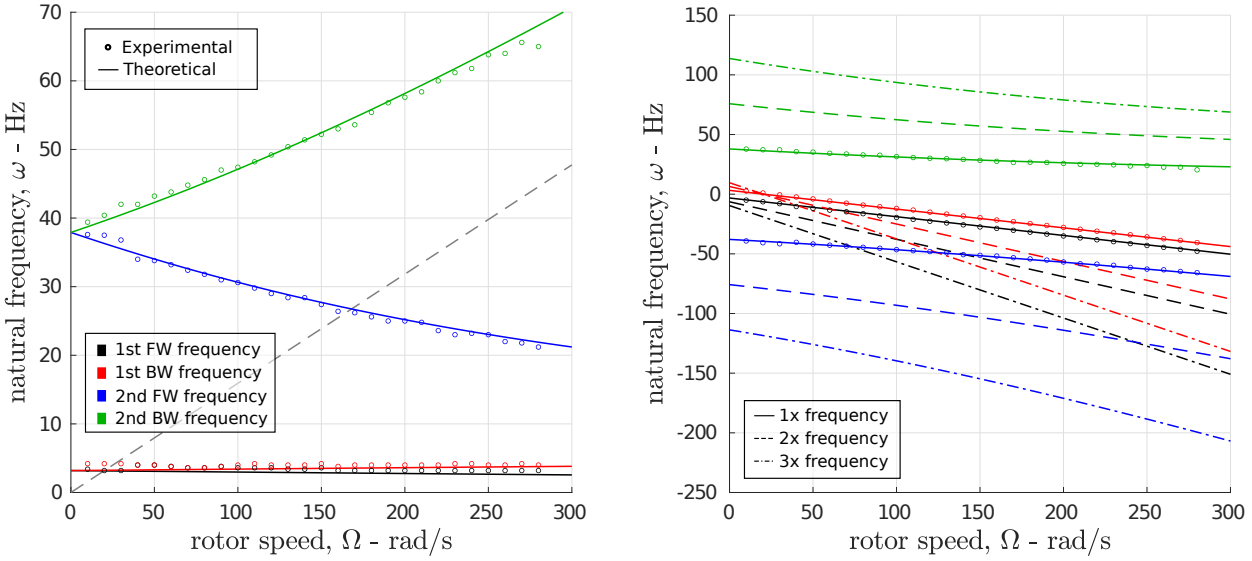

Figure 6: Classical (left), rotating-frame (right) signed Campbell diagram [21]. Both Theoretical calculation and the experimentally measured values are plotted. Legends apply to both figures and complete each other.

4.3. Obtaining the nonlinear force-displacement curve of the stator

The force-displacement curve of the stator restoring force was measured and a cubic polynomial was fitted for high and low tightness of the rotor. The photograph of the force-displacement measurement kit made up of extrusion segments can be found in Figure 7. The handle in the middle moves along the rail and pushes against two compression springs, each of $k = 4378$ N/m. The springs push the stator laterally. The MTI sensor tracks the position of the handle, denoted x_{MTI}, while Omron sensors (OG and OW) track the position of the stator by their average, $x_{Omron} = (x_{OG} + x_{OW})/2$. The force exerted on the stator is, therefore, $f = 2k\left(x_{MTI} - x_{Omron}\right)$. To prevent the effect of the shaft bow on the stiffness calculation, the bow was positioned perpendicular to the force-displacement kit axis at the time of the measurements. Although the force-displacement curve was only taken in one direction, due to the isotropy of the system it is reasonably assumed that the response will be equal in all directions.

The nonlinear force in the system is very sensitive to the amount of tightness of the stiffness rods. Their tightness is achieved with M3 nylocks and M3 locknuts, as illustrated in Figure 8. The bottom 135 bearings of the rods are sandwiched tightly between two M3 Nylocks. The upper 135 bearing of the rods are tightened only from the upper side with the help of one nylock and one locknut. The tightness on all of the rods was managed in an iterative way, while at the same time keeping the stator level.

A cubic polynomial regression is applied to the lateral force in Figure 9. The cubic term in the full cubic regression is not affected by any shift of the data in the x-y plane of the plot. Additionally, the cubic term in the cubic regression without the quadratic term is not affected by vertical shift. Therefore, the cubic regression must be reliable even with a slight data shift present in the measurement data. Two different cases are presented: a higher tightness on the stator (Figure 9a), and a low tightness on the stator (Figure 9b). In the higher tightness case (Figure 9a) the full cubic polynomial fit gives 0.1557 N/mm^3 (red), whereas the cubic fit without quadratic term gives 0.2044 N/mm^3. In the low tightness case (Figure 9b), the full cubic polynomial fit gives 0.1631 N/mm^3, whereas the cubic fit without quadratic term yields 0.1571 N/mm^3. Both in Figure 9a and 9b, the cubic regression without quadratic term represents the force-displacement data well; therefore, quadratic term is not used.

5. Results and Discussion

In this section the results in the form of bifurcation diagrams from both experiments (Section 5.1) and simulations (Section 5.2) are given, as well as selected relevant orbits representing different branches. Section 5.2 also compares simulation to experiments and comments on the concordance and discordance between the two.

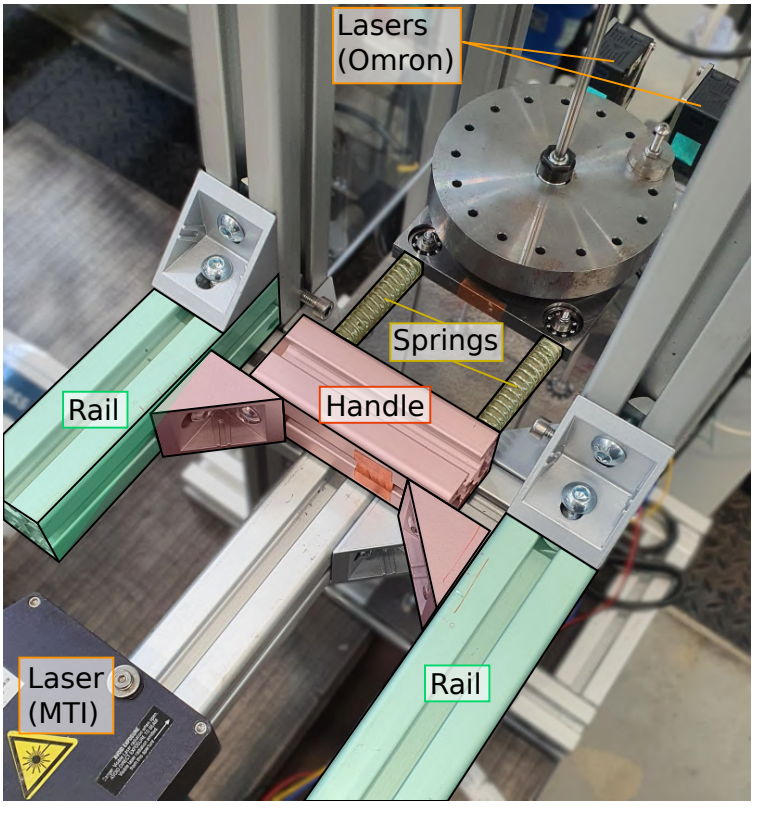

Figure 7: The force-displacement curve measurement kit installed on the rig.

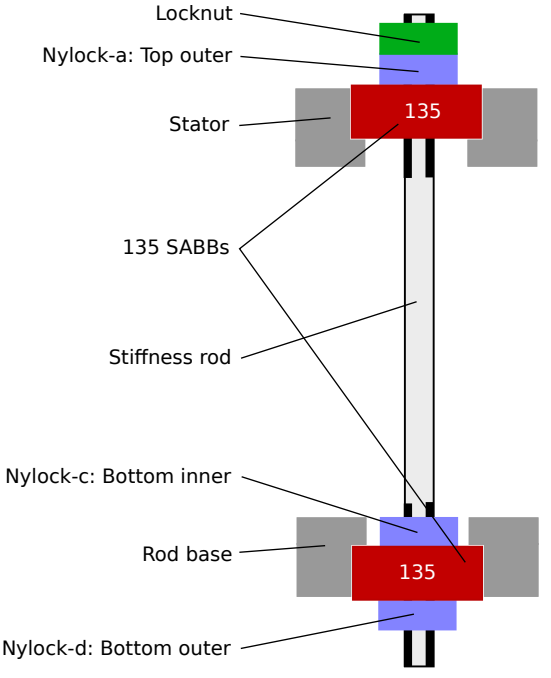

Figure 8: Schematic drawing explaining the tightening of the stiffness rods. '135' refers to the catalogue names of these self-aligning ball bearings.

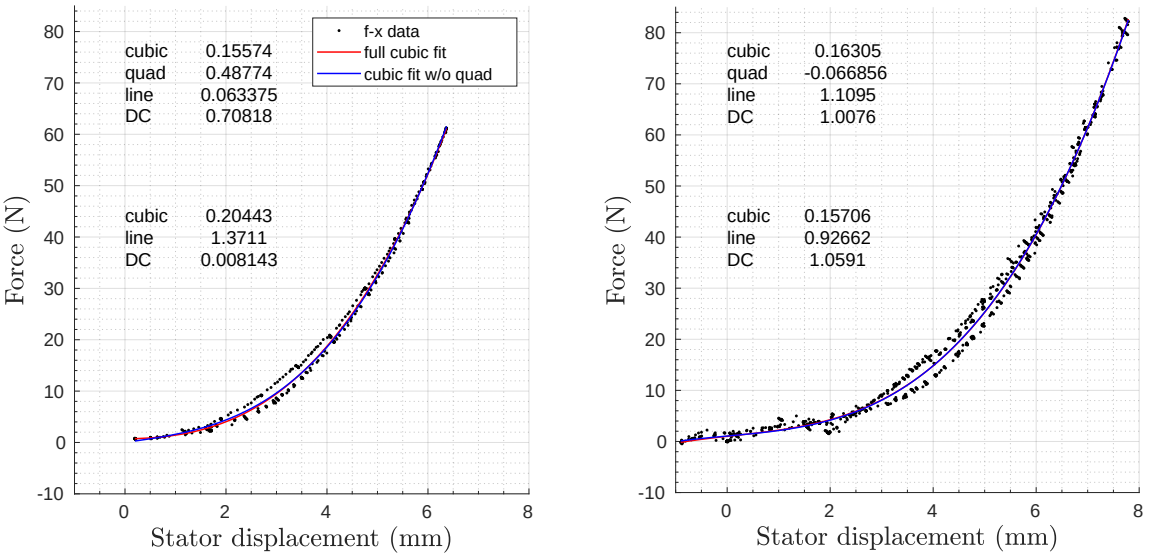

(a) Data for higher level of tightness

(b) Data for low level of tightness

Figure 9: Force-displacement data from different measurements. Legend applies to both figures.

5.1. Experimental bifurcation diagram

Figures 10 and 11 show an experimental bifurcation diagram (BD). At each data point, the motor speed was set and time was allowed for the rig to reach a steady state of vibration. For cases other than simple synchronous whirling, it was necessary to activate the response with an impact applied manually to the stator. The main resonance experiences the jump phenomenon due to stiffening from the cubic stiffness. Therefore, as the slow runup was performed in a stepped sine fashion, after jump-down on the main resonance, the jump-up point was sought by decreasing the speed control voltage. Once a particular response was obtained, the motor speed control voltage was gradually changed to explore the branch, in a similar manner to a stepped sine test. A rich variety of different responses are observed, as discussed in the following subsections. Some of the responses have been excluded from the commentary and dubbed 'outliers' in Figure 10 due to capturing the irrelevant transient response after the stator is impacted or because of the mode's disengagement.

5.1.1. 2^1:1^1 internal resonance

The largest branch of responses has a minimum drive speed of 56 rad/s. These responses are quasiperiodic in the stationary frame, but form periodic orbits with 2:1 resonance in the rotating frame as seen in [29, 28, 22]. A typical example of this 2:1 response is given in Figure 12, where the stroboscopic samples trace the rotating frame orbit which shows the characteristic single loop shape. The fast Fourier transform was taken on the x-y plot data represented as a complex coordinate $x + jy$ where $j = \sqrt{-1}$ resulting in the frequency spectrum in the right of Figure 12 where the FW/BW frequencies are in the positive/negative axis. The frequency content shows three distinct peaks, relating to the 1st pair of FW and BW whirl modes and the drive speed, hence it is denoted 2^1:1^1 (see Eq. (1) and (2) and the explanation thereof).

It was very difficult for this mode to hold consistently between 65-97 rad/s: At a certain orientation of the precession, the stator started to vibrate torsionally, following which the 2^1:1^1 mode was lost. Figure 13 shows that there was a noticeable precession orientation where the precession speed is slow and the trajectory covers the space more densely. However, below 65 rad/s and above 97 rad/s, the mode started to hold well again, while the preferred orientation became less pronounced.

Sometimes, the orbit was completely *parked* in only one orientation, as in Figure 14, and the frequency content shows that the orbit is periodic in both stationary and rotating frames. The stroboscopic Poincaré section in Figure 14 shows three dots, indicating a one-to-three ratio between the drive speed and the other main frequency components in the stationary frame: $3\,|\omega_f^{sta}| = 3\,|\omega_b^{sta}| = \Omega$ (see the right hand side of Figure 14). This shows that this parked 2:1

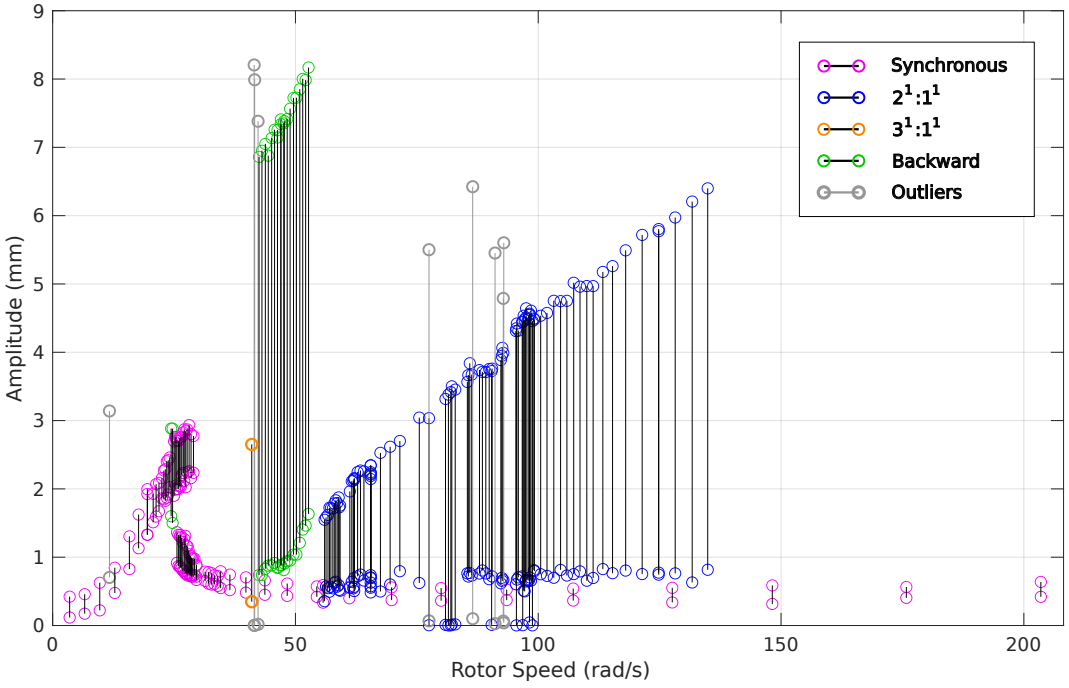

Figure 10: Experimental BD showing the amplitudes of stator lateral motion with drive speed. Maximum and minimum amplitudes of each family is given the same colour.

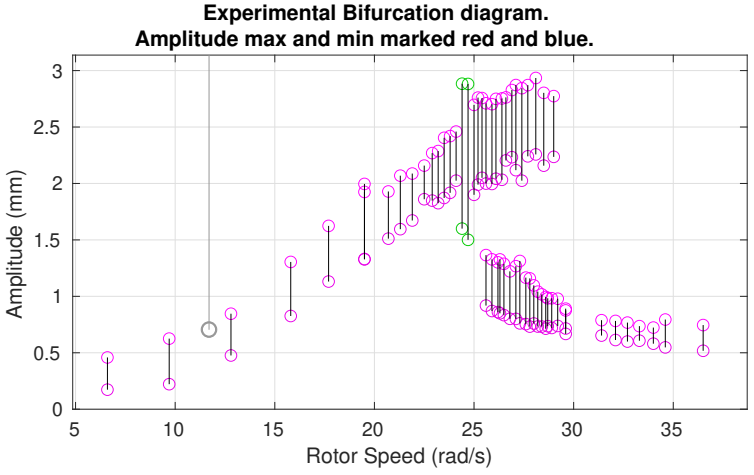

Figure 11: Zoom at the main resonance of the BD. Legend in Figure 10.

response in the stationary frame is a period-3 motion, not a quasiperiodic motion unlike other 2:1 responses on the same branch. This happens while the rotating frame frequencies still show a 2:1 ratio between the FW and BW frequency components: $2\,\omega_f^{rot} = \omega_b^{rot}$. The reason for parked orbits or the preferred orientation of the trajectory might be related to the stiffness rods having marginally different lengths and damping characteristics. Additionally, their tightening to the same tightness was a practically difficult task. This might have caused the $3^1{:}1^1$ IR mode to be parked (Figure 15), as well.

The experimental setting with overhung rotor and cubic smooth nonlinearity has not been encountered in the experimental literature. However, Ishida et al. [35] confirmed in an analytical HBM and experimental study on a slender shaft that symmetric nonlinearity such as cubic nonlinearity can generate $2\,\omega_f^{sta} - \omega_b^{sta} = \Omega$, which is the 2:1

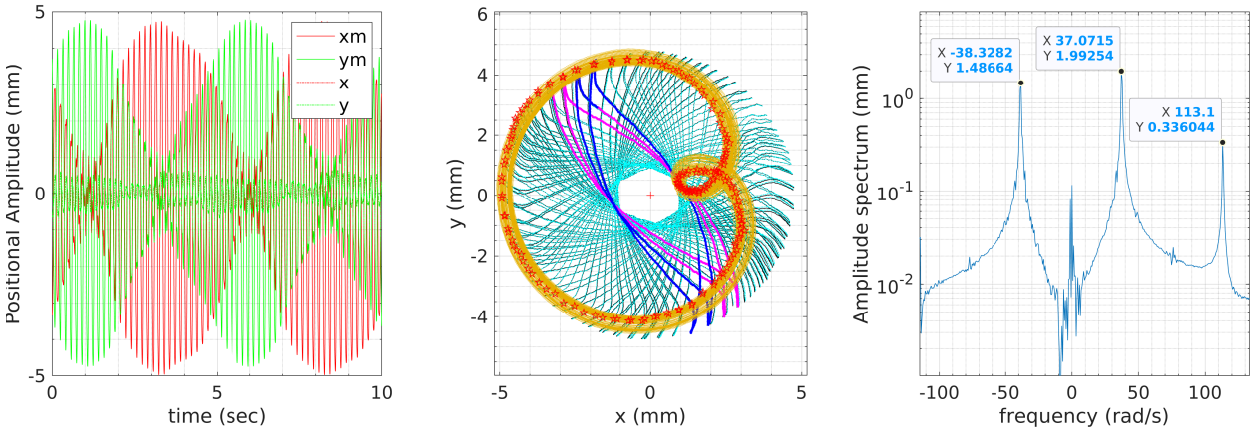

Figure 12: IR of type $2\,\omega_{f1}^{rot} = \omega_{b1}^{rot}$ at $\Omega = 113.3$ rad/s from the experimental BD in Figure 10. See legend for middle figure in Table 3.

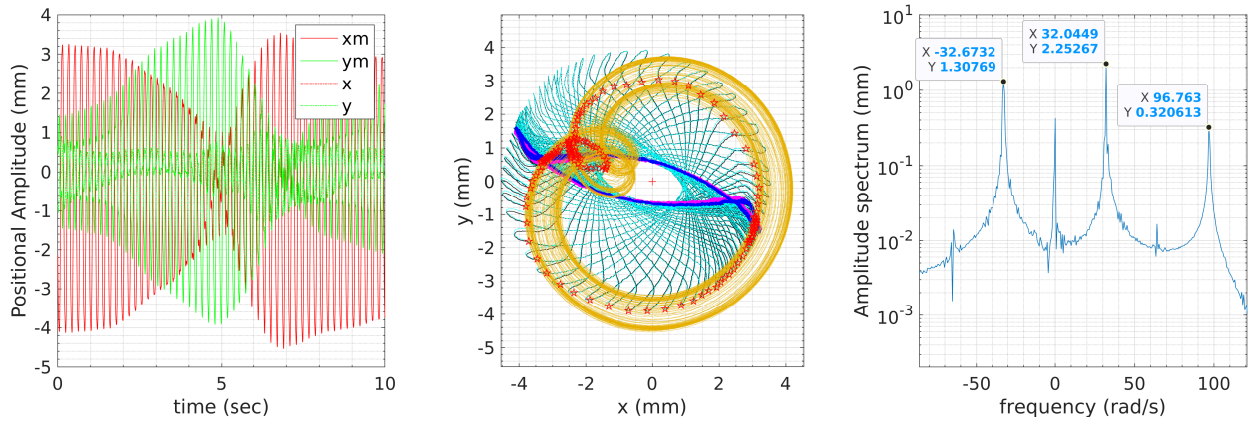

Figure 13: A sample $2^1{:}1^1$ orbit at $\Omega = 97.0$ rad/s that shows the preferred orientation. See legend for middle figure in Table 3.

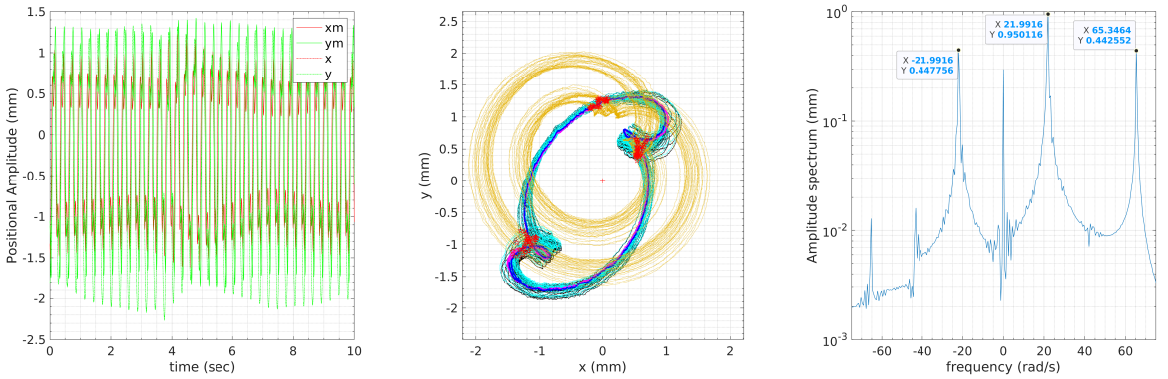

Figure 14: A sample $2^1{:}1^1$ orbit at $\Omega = 65.5$ rad/s that shows that the trajectory is not precessing, but rather *parked*, and the orbit is periodic in both stationary and rotating frames of reference. See legend for middle figure in Table 3.

IR observed here. This response was also seen in the extended Jeffcott rotor experiments [15]. IRs of 1:(−1) type are investigated in [37] which was excited thanks to the symmetry breaking effect of gravity forces. Ref. [24] investigated stochastic FEM rotor-stator rub impact and stated that response variance is high in IR compared to main resonance.

Table 3
Legend that applies to Figures 12-17 and 23.

Line feature		Explanation
——	black line	Measurements (x_m, y_m) from sensor readings
——	cyan line	Deciphered stator trajectory in (x_s, y_s) stationary frame (Eq. (A.1))
——	pink line	First 1500 data points
——	blue line	Second 1500 data points
★	red stars	Stroboscopic Poincaré section for the duration of the measurements
·····	yellow trajectory	Rotating frame view of cyan line

5.1.2. 3^1:1^1 internal resonance

In previous studies [29, 55], a branch of solutions that are quasiperiodic in the stationary frame but 3:1 internally resonant and periodic in the rotating frame have been seen. However, in this experiment there is only one IR response with $3\,\omega_{f1}^{rot} = \omega_{b1}^{rot}$ frequency relation observed during the experiments which exhibit a parked orientation (see Figure 15). It appears as a period-2 motion, i.e., with two localised dots in the stroboscopic Poincaré section, due to the commensurate frequency ratios in the stationary frame: $2\,|\omega_f^{sta}| = 2\,|\omega_b^{sta}| = \Omega$ (see in the right hand side of Figure 15). Note that this happens when the rotating frame frequency ratio for the 3^1:1^1 response still holds: $3\,\omega_f^{rot} = \omega_b^{rot}$. Hence, the response is periodic in both frames. The difficulty of obtaining 3:1 IR responses was established in [29] compared to 2:1 mode which is impacted less by damping compared to 3:1. Though uncommon, Ref. [23] numerically observed 3^2:1^2.

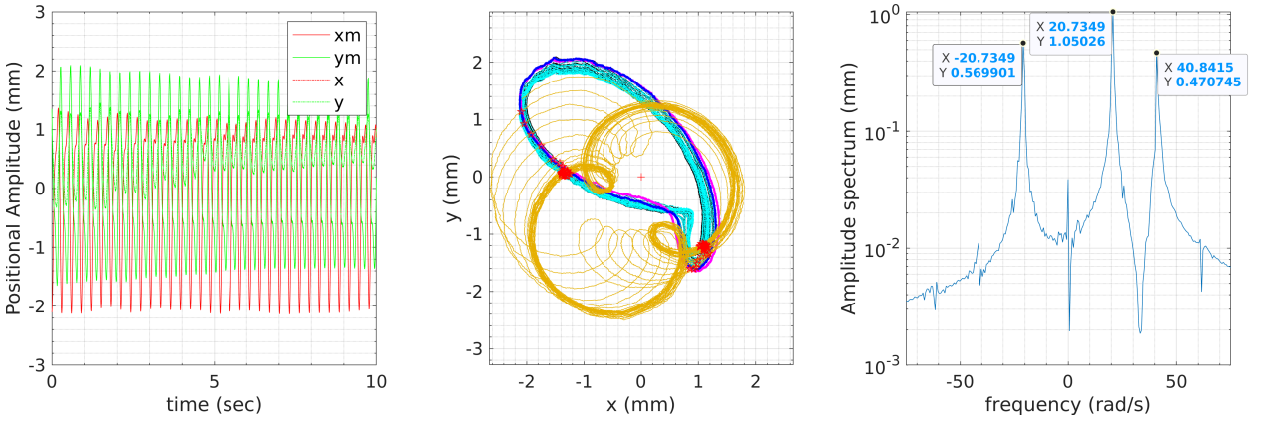

Figure 15: IR of type $3\,\omega_{f1}^{rot} = \omega_{b1}^{rot}$ $(3^1{:}1^1)$ at $\Omega = 41.0$ rad/s which appears periodic in both the rotating and the stationary frame. See legend for middle figure in Table 3.

5.1.3. Self excited backward resonance

The highest amplitude branch of solutions, occurring at around 50 rad/s in Figure 10, is of a form seen typically in contacting rotor systems where friction is present [27, 22, 30, 41]. The axial loads increased damping in the bearings holding the stator, which must have excited the friction-related backward motion. This feature was not modelled in the theoretical part of the present study. Interestingly, however, this response can be predicted by a novel backbone analysis [26] performed systematically on the underlying conservative system.

Two examples of this response are shown in Figure 16, where it can be seen from the stroboscopic samples that the rotating frame orbit is a simple loop, unlike the tear-drops in a model with impacts [30]. Here, the forward whirl

components' frequency matches the drive speed, while backward whirl mode is excited and creates an oscillation that again is quasiperiodic in the stationary frame, yet periodic in the rotating frame. The frequency spectra show just two significant peaks (unlike 2:1, which shows three), because the forward mode and drive speed components are at an identical frequency, while the backward whirl mode adds a second, negative, frequency. This resonance is not evident from the Campbell diagram in Figure 6 because this is not an internal resonance. The formation of this response near the main resonance is discussed further later.

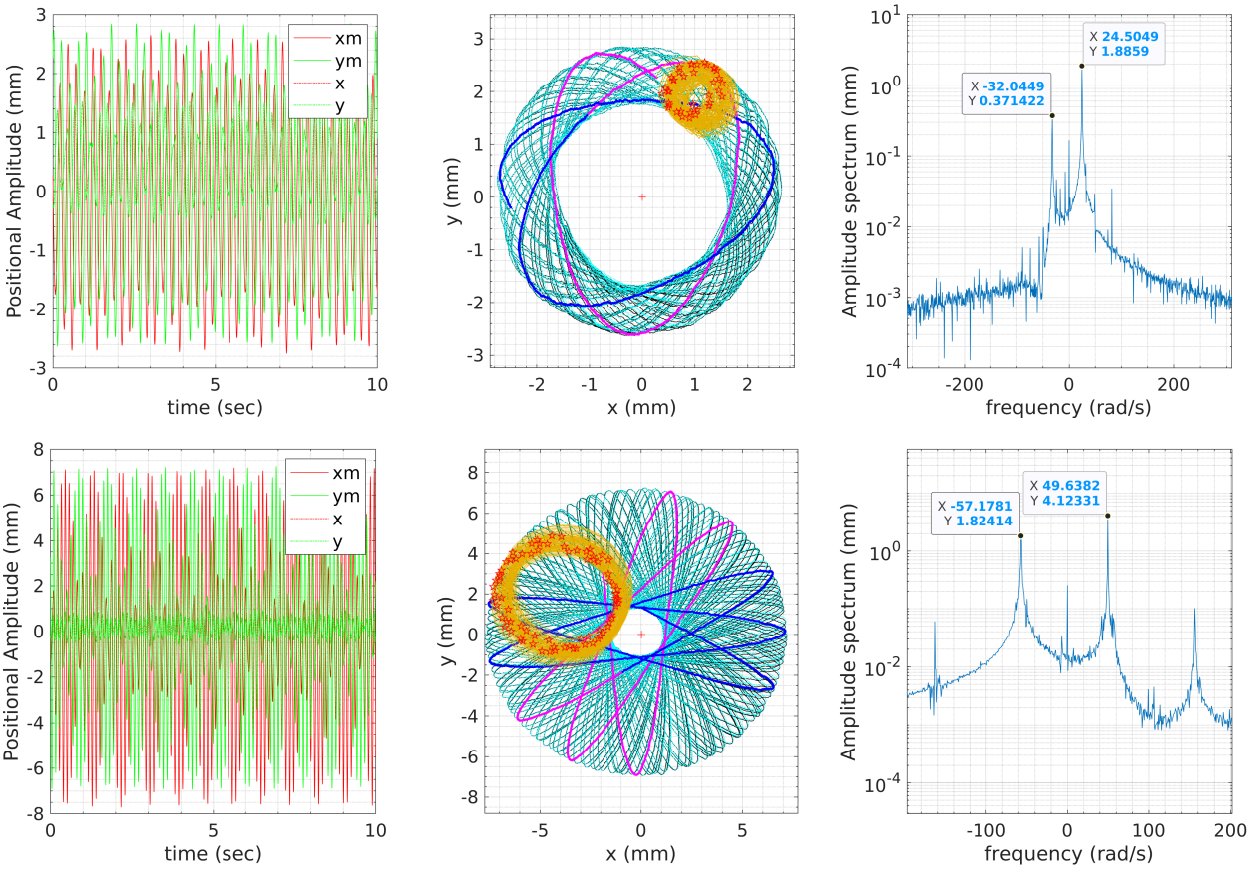

Figure 16: Two samples of quasiperiodic self excited BW resonance which also appears periodic in the rotating frame at $\Omega = 24.7$ rad/s and at $\Omega = 49.6$ rad/s from top to bottom (see the BD at Figure 10 and 11). See legend for middle figure in Table 3.

5.1.4. Synchronous response

Due to the stiffening effect of the cubic stiffness, the synchronous response shows jump phenomena (Figure 11). The jump down and jump up happens at 29.0 rad/s and 25.6 rad/s, respectively. Some of the synchronous responses from Figure 11 are shown in Figure 17. The deviation of the stator position (—) from the measured (—) data is visible in the supercritical low amplitude orbit after jump down at 32.1 rad/s and at high speed at 203.5 rad/s. This is attributed to torsion on the stator by a low level of friction in a 2305 bearing. The synchronous responses deviate slightly from perfect circles around the main resonance region. This could be attributed to some weak anisotropy in the stator support stiffness. At high speed, the response looks very noisy due to the bearing clearances and vibrations of the rods.

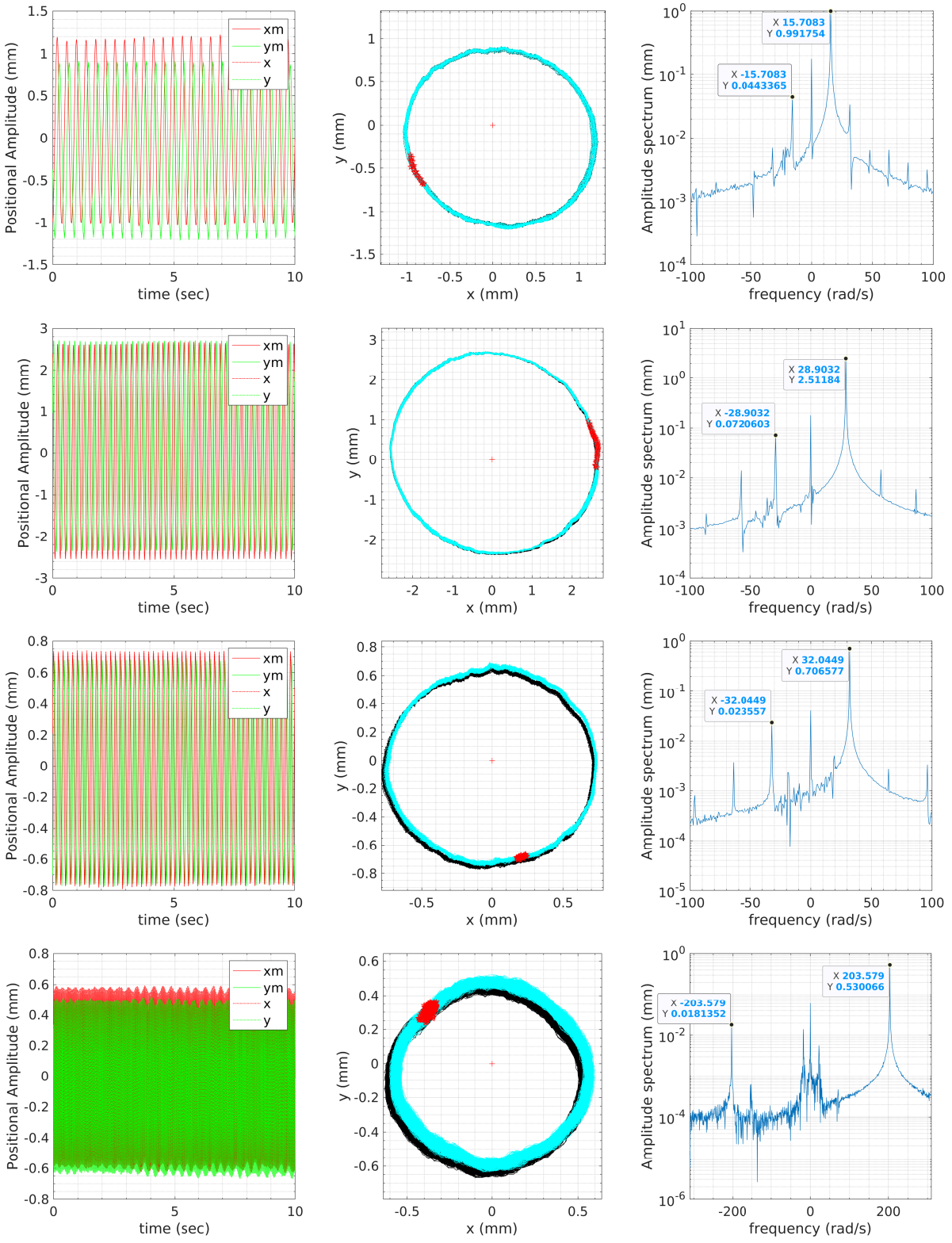

Figure 17: Selected orbits at Ω = 15.8, 29.0, 32.1 and 203.5 rad/s from top to bottom, from the BD given in Figure 10 and 11. See legend for middle figure in Table 3.

5.1.5. Main resonance

The experiment featured a bounded main resonance peak as shown in Figure 11. Around the main resonance the response would oscillate between round, elliptical and self-excited backward resonance modes, not settling even after several minutes.

In order to investigate whether the main resonance peak has a hard drop-down limit due to modal interactions in the main backbone, a comparison between low and higher unbalance was studied. The test setup was disassembled before this was done for more accurate mass measurements. The reassembly created a slightly different system. The results are shown in Figure 18. Higher unbalance causes higher response amplitudes, as expected. However, in the case of higher unbalance, the main resonance peak is obliterated by the self-excited backward resonance which attracts all nearby trajectories. Chipato et al. [22] observed this response growing from the main resonance. Shaw et al. [26] shows that the self-excited backward resonance can become more stable than direct synchronous whirling under the right circumstances.

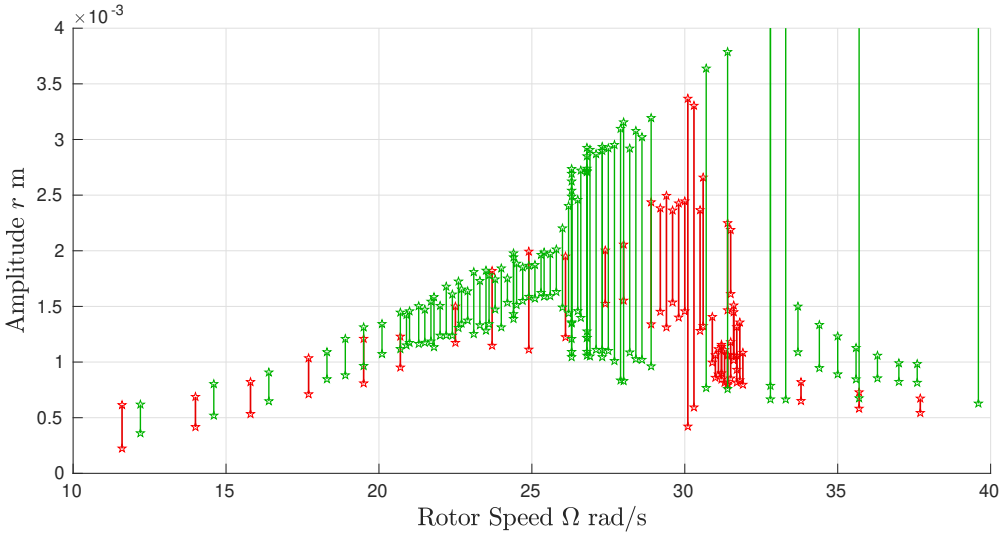

Figure 18: Comparison between the region of the BD around the main resonance with different unbalance masses. The red coloured data belong to the run with an unbalance mass of 19.46 g (Note that this is different than Figure 11). The green coloured data belong to the run with an unbalance mass of 28.87 g.

In the formation of self-excited backward resonance around the main resonance, different explanations can be made. It could have directly resulted from the amplitude dependent friction in the bearings holding the stiffness rod, as mentioned above for the higher amplitude self-excited backward resonance. Slight anisotropy due to the stiffness rods already created slightly elliptical orbits near the main resonance which turned into self-excited backward resonance more easily due to friction. Another possible explanation concerns the gyroscopic effects being small for the first pair of modes (see Figure 6). Inoue and Ishida [58] showed that in the presence of lower gyroscopic effects and slight anisotropy, the 1:-1 IR that is expressed between the stationary frame modal frequencies gives rise to a Hopf bifurcation of the amplitude of the steady state response around the main resonance. The study [58] did not feature frictional interaction unlike the experiments here, but it had a form of anisotropy which was the cause of the excitation of the negative frequency that is near the negative drive speed component. In terms of the frequency content, the resulting quasiperiodic 1:-1 IR motion due to anisotropy in [58] appears the same as the self-excited backward resonance around the main resonance in the present study.

5.2. Simulation bifurcation diagram and comparison to experiment

The BD obtained from the time simulations of the system in Eq. (20) with the parameters defined in Eq. (21) is given in Figure 20a which was supported with partial sine-sweep tests (up or down) on the synchronous response and on the IR responses of $2^1{:}1^1$ and $3^1{:}1^1$. The figure also included the experimentally obtained BD from Figure 10 for comparison.

5.2.1. Values from the assembled rig

After the manufacture of the whole rig, the masses, dimensions and positions are measured to be used in time simulations, which were slightly different compared to the design due to the material differences, assembly process and connecting elements such as nuts and bearings. For accurately capturing the inertial properties, a “disk system" is defined which included the disk itself, the moving parts of the bearings of the stator, the stator sleeve for collet, the collet and lockbush, and the shaft around the disk (see Figure 19). The data in Eq. (21) were used in the Campbell plot and in simulations. Misalignment was not included which did not cause any noticeable effect in the BD of the unbalance response (see Table A.1). The link between stator and the disk was assumed to be rigid since a 30 mm disk-stator distance in the design decreases to only 10 mm open shaft material in the manufactured rig.

$$E_1 = 230\ \text{GPa} \qquad I_1 = 30.69\ \text{mm}^4 \qquad a = 268.91\ \text{mm} \tag{21a}$$
$$d_1 = 5\ \text{mm} \qquad d_2 = 3\ \text{mm} \qquad b = 30.51\ \text{mm} \tag{21b}$$
$$\varepsilon_u = 45\ \text{mm} \qquad \beta_u = 0 \qquad \delta_u = \gamma_u = 0 \tag{21c}$$
$$\varepsilon_b = 0.5(a/L_1) = 0.45\ \text{mm} \qquad \beta_b = \varepsilon_b/L_1 = 86.0\ \text{m deg} \qquad \delta_b = \gamma_b = 0 \tag{21d}$$
$$m_d = 1593.89\ \text{g} \qquad m_u = 19.46\text{g} \qquad m_s = 750.43\ \text{g} \tag{21e}$$
$$k_{rb} = 926.62\ \text{kN/m} \qquad c_{rb} = 0.516kN/(m/s) \qquad k_{3b} = 157061\ \text{kN/m}^3 \tag{21f}$$
$$J_d = 1639.366\ \text{kg mm}^2 \qquad J_p = 2236.895\ \text{kg mm}^2 \tag{21g}$$

where d_1 and d_2 are the shaft and the stiffness rods' diameters.

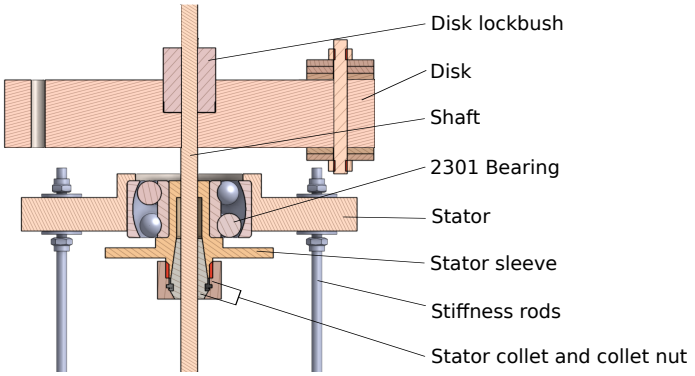

Figure 19: The disk system that interprets the rotating parts as a single rigid system: the disk, the stator sleeve, the bearing moving parts and the connecting elements (collet and lockbush), as well as the shaft length around the disk (80 mm before and 177 mm after the disk, total 277 mm shaft length).

5.2.2. Simulation bifurcation diagram

The two BDs are broadly similar in shape, with the exception that for the experimental BD there is an additional region of backward whirl response not modelled numerically, and the SS response is bounded (see Figure 18). These differences are attributed to the increased damping in the bearings with axial load. Additionally, in the IRs $2^1{:}1^1$ and $3^1{:}1^1$ that appear in the simulations, the Campbell diagram values for IR frequency estimation from Table 2 are followed well. However, the BD features of the experiments appear systematically lower in the rotor speed range. Although the experimental Campbell diagram from tapping tests is very similar to that of the theoretical Campbell diagram from the experimental rig values (Figure 6), it is worth noticing the shallow angle between the intersecting lines in Figure 6. This means that these lines' points of intersection, which govern onset drive speeds of IR, will be highly sensitive to small changes in the modal frequencies or even in the gyroscopic effect on the frequency that might have been altered by the axial pull of the stator. Therefore, any effect on the Campbell diagram can shift the position of the IR branches in the Ω axis significantly. This might also be related to the fact that the 7900 angular contact ball bearings cannot provide a perfectly rigid support, which alters the effective shaft length. Combining the above, the location of the 2:1 branch in the rotor-speed axis is very close: the experimental branch appeared at 56 rad/s, while the theoretical one appeared at 65 rad/s, at their lowest tips which is where the Campbell diagram values predict. This discussion above

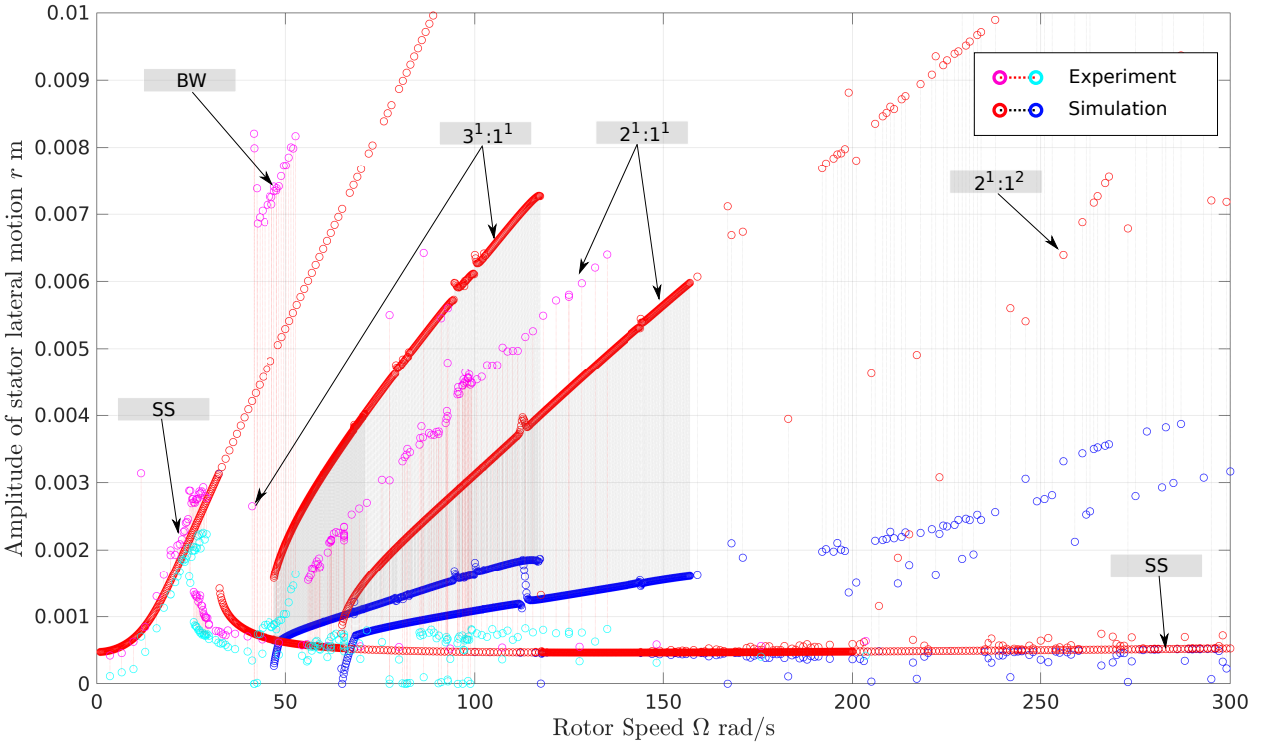

(a) Experimental BD from Figure 10 merged with the simulation results.

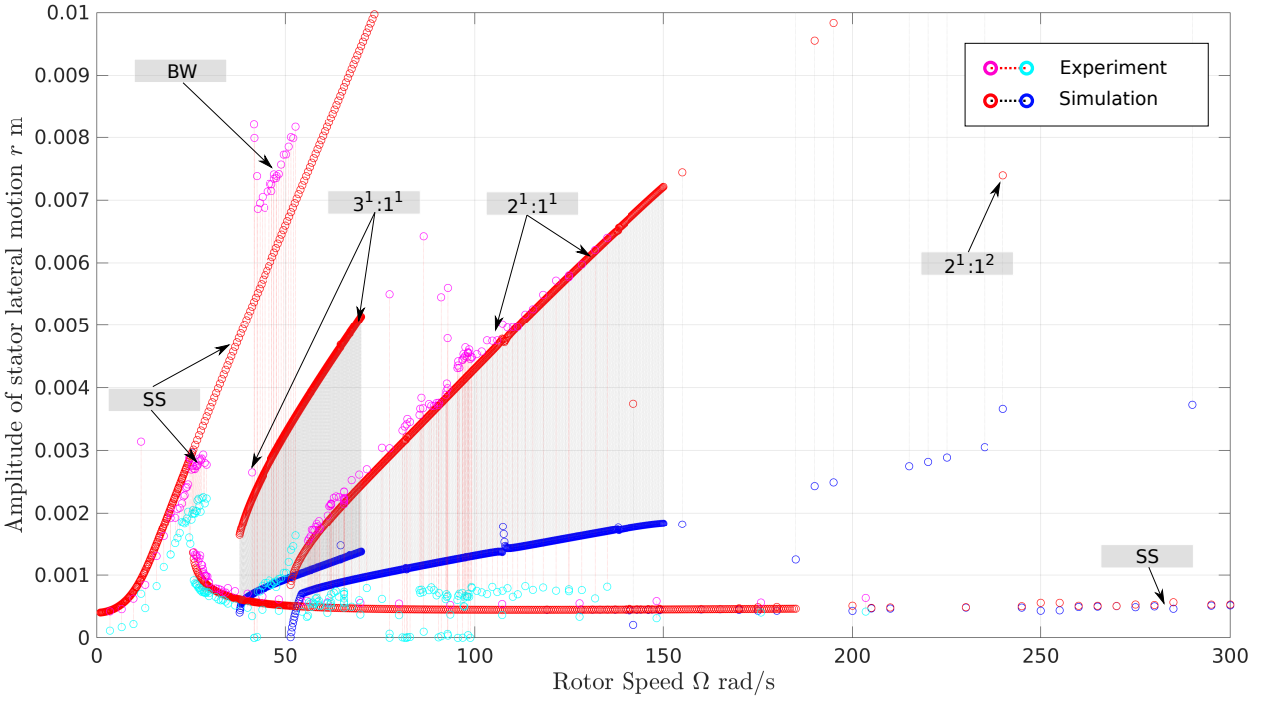

(b) Experimental BD from Figure 10 merged with the simulation with the following modifications to Eq. (21) values: $E_1 = 270$ GPa, $k_{3b} := 0.7\,k_{3b} = 109942700$ N/m^2, and with the addition of the 7900 bearing's movement compensation as the extra shaft length $D = 65$ mm. (See Figure B.1 for the linked Campbell plot.)

Figure 20: Experimental and simulations BDs.

also explains why the IRs in the experimental and theoretical BDs must not be compared in amplitude, but in the x-axis of the BD. Therefore, the aim of the experiment being the regeneration of the theoretical IR phenomena was fulfilled by the experiments implemented as shown in the present work. However, slightly different test rig parameters can give a much closer match as illustrated in Figure 20b, indicating the sensitivity of the BD to the test rig parameters which in this case was not manufactured to be a high fidelity representation of the mathematical 4-dof model.

There are other factors such as the temperature of the test environment that affected the force-displacement measurements by around 20% (see Figures 9a and 9b and the force difference thereof). However, this would rather influence the inclination of the experimental $2^1{:}1^1$ branch instead of directly affecting its position along the BD. Since the presented experimental run had a very low level of tightness, the value chosen for the cubic stiffness in the experiments was 0.15706 N/m^3 which was derived from the force displacement curve in Figure 9b. This value appears to be legitimate because the inclination of the resulting experimental 2:1 branch is matched well by that of the theoretical simulations throughout the branches covering their respective ranges of amplitude of motion for the parameters chosen.

During the experiments, the IR of the 1st FW mode (swinging of the disk) with the 2$_{nd}$ BW mode (angling of the disk), named $2^1{:}1^2$ was not observed. The basin of attraction of this mode was small. When the rotor was rotating with high speeds (e.g. 250 rad/s), it was keeping its angle thanks to high angular momentum despite the external impacts. It was readily achieved in the simulations, though only when the viscous damping constant was decreased to lower values.

Interestingly, both IR branches of $2^1{:}1^1$ and $3^1{:}1^1$ exhibit a stationary frame periodic solution, which is named here as *stagnation* and does not appear in the literature to the knowledge of the authors. Above that rotor speed the precession of the trajectory appears BW whirling and below FW whirling, i.e., filling the configuration space in these directions. This is illustrated in Figure 21 for 2:1 and Figure 22 3:1 IR. At first glance, these are similar to the parked orbits of the same resonance from the experiments (Figure 14 for $2^1{:}1^1$, Figure 15 for $3^1{:}1^1$). As a result, the same discussion on their appearance as period-3 for $2^1{:}1^1$ and period-2 for $3^1{:}1^1$ IR is relevant from Section 5.1. However, while stagnation is a reflection of the physical phenomena and happens at a particular rotor speed for a given IR branch in both experiments and the time simulations, the parked orbits are the result of the imperfect experimental conditions and happened at various speeds.

The only achieved $3^1{:}1^1$ response in the experiment was a parked trajectory, i.e. appeared without any precession. There is not a complete $3^1{:}1^1$ branch data from the experiments. The complete branch data for $3^1{:}1^1$ resonance was already difficult even with lower damping values used in the simulations: only one solution was found which was sine-swept slowly (0.1 rad/s at a time) up and down the rotor speed. In that case, it is not obvious whether the only $3^1{:}1^1$ response found experimentally was truly found stagnant, as in the simulations (Figure 22) or whether it is only parked in that orientation due to other unknown effects such as support anisotropy.

The stagnation phenomenon is illustrated in Figure 23 with the orbits from the experiment. Figure 23a shows a low speed orbit that is precessing in the FW direction, as expected from the above discussion on the simulation results. However, the parked $2^1{:}1^1$ experimental orbit in Figure 23b did not happen at the stagnation where the transition from FW to BW precession happens. Therefore parking phenomena is separate to stagnation.

Figures 23c and d show the trajectories right before and after the experimental stagnation happens. The FW precession of the experimental $2^1{:}1^1$ was present up to 69.5 rad/s (Figure 23c) which changed to BW at 71.5 rad/s (Figure 23d). However, until around 100 rad/s, the orbits were not easily sustained: once the stator started vibrating, the IR was lost, which was linked to the possible effect of slightly unequal force profiles from the stiffness rods in the experiment. This means that during low speeds of FW or BW precession, the stator vibrations are excited which interferes with and disengages the $2^1{:}1^1$ IR. This effect was more pronounced for the BW precessing (i.e. above stagnation) orbits. However, as the BW precession speed increases, the stator vibrations are damped/overcome more easily and the mode remains locked.

6. Conclusion

A cantilever overhung rotor was designed that is comparable in dynamics to those used in [29] and [55]. A stator that is connected to the shaft and linked to the ground with a pinned-pinned boundary condition was designed. A set of 4-dof equations of motion was developed where the degrees of freedom are the stationary frame lateral displacements of the disk and the two angular displacements of the disk about the two lateral axes. Note that this design is easily adaptable to a stator that features a contact nonlinearity rather than a soft nonlinearity. The attention is paid to the

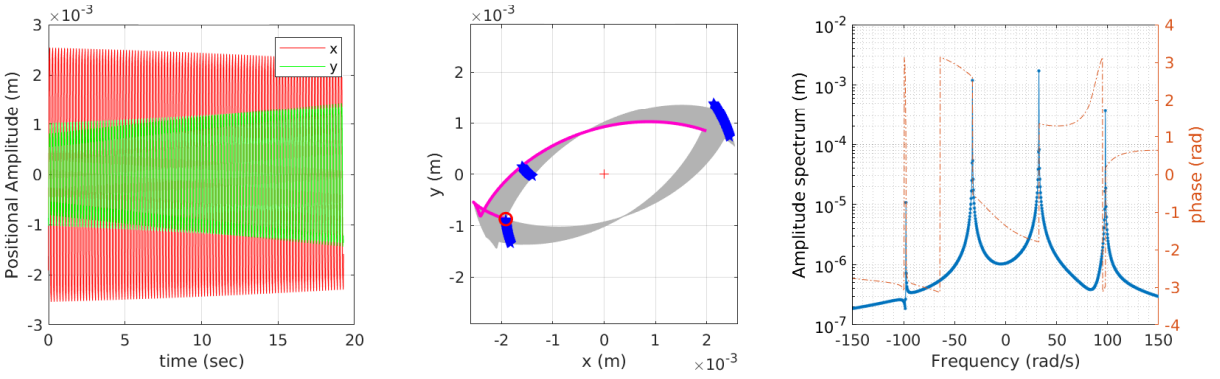

(a) $\Omega = 97.8$ rad/s, FW precessing trajectory.

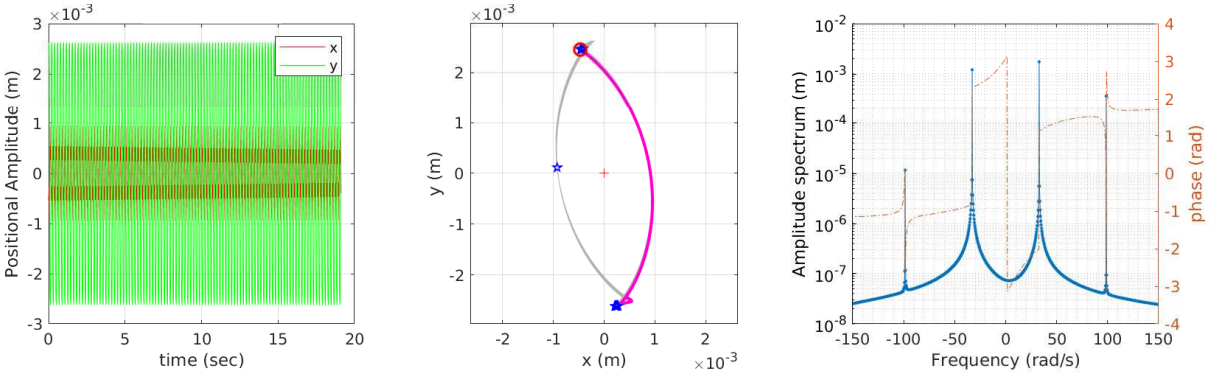

(b) $\Omega = 98.6$ rad/s, stagnant trajectory.

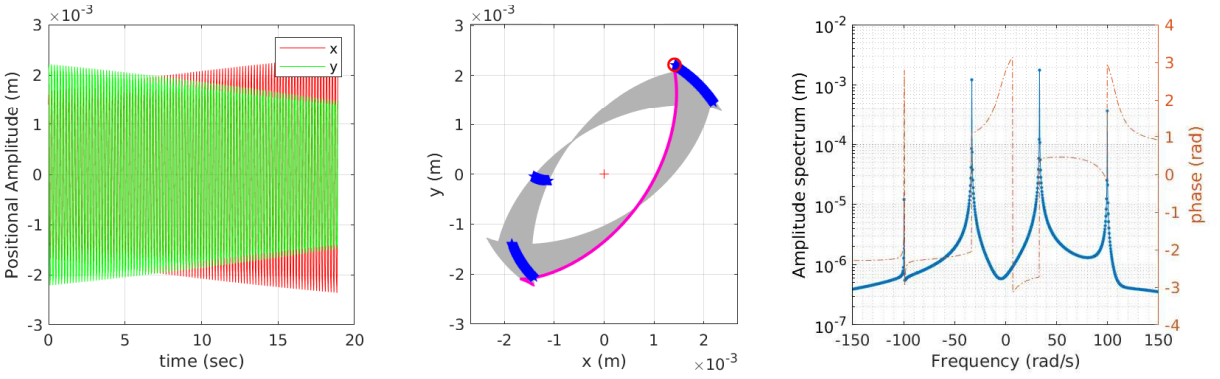

(c) $\Omega = 99.6$ rad/s, BW precessing trajectory.

Figure 21: The stagnant (period-3) orbit on the quasiperiodic 2^1:1^1 branch from time simulations. In the middle column: The pink orbit shows one quasiperiod (i.e. one repeating, precessing pattern). Blue pentagrams show the stroboscopic Poincaré section. Gray line is the trajectory of the stator that covers the time of 200 pink orbits.

theory-practice link by establishing comparable dynamics to a purely theoretical system [19] and to the preceding works [29, 55]. The importance of a proper DAQ system is stressed.

This work is the first comprehensive experimental demonstration that cubic geometric nonlinearity alone (without contact) can generate complex internal resonance responses including 2:1 and 3:1 modes, forward-to-backward precession switching, and mode-locked behaviours previously attributed primarily to contact nonlinearities. It also aims to establish a valuable research tool for the rotordynamics community with a versatile experimental platform for future investigations, while pointing out the practical aspects to take into consideration for such experiments including the influence of shaft bow, bearing friction, support anisotropy and unbalance level on the nonlinear response.

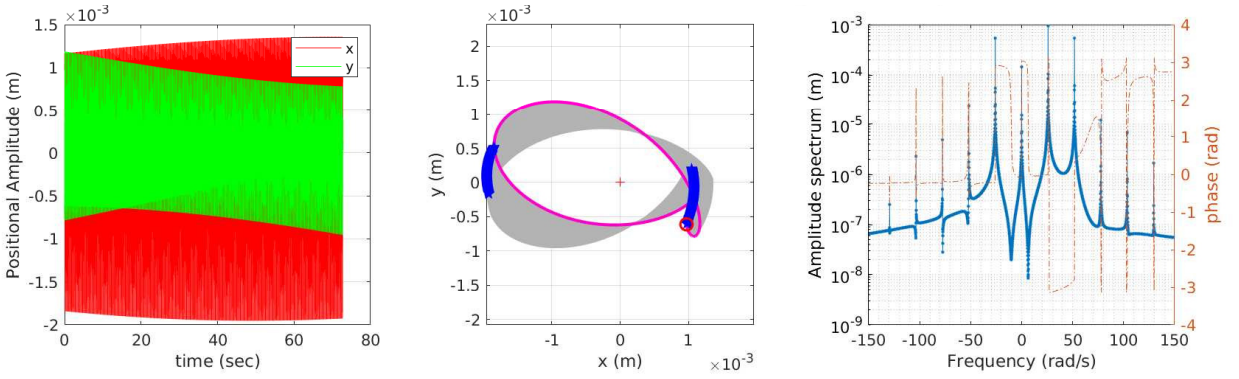

(a) $\Omega = 51.8$ rad/s, FW precessing trajectory.

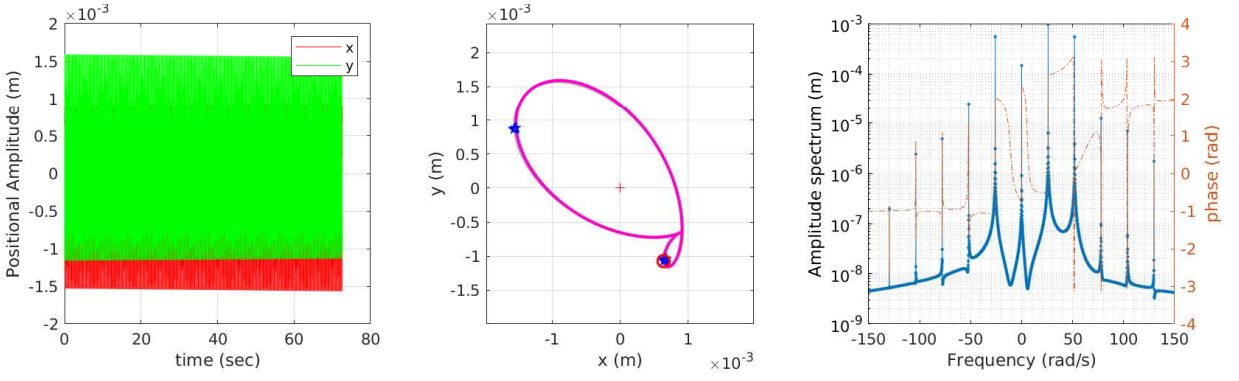

(b) $\Omega = 51.9$ rad/s, stagnant trajectory.

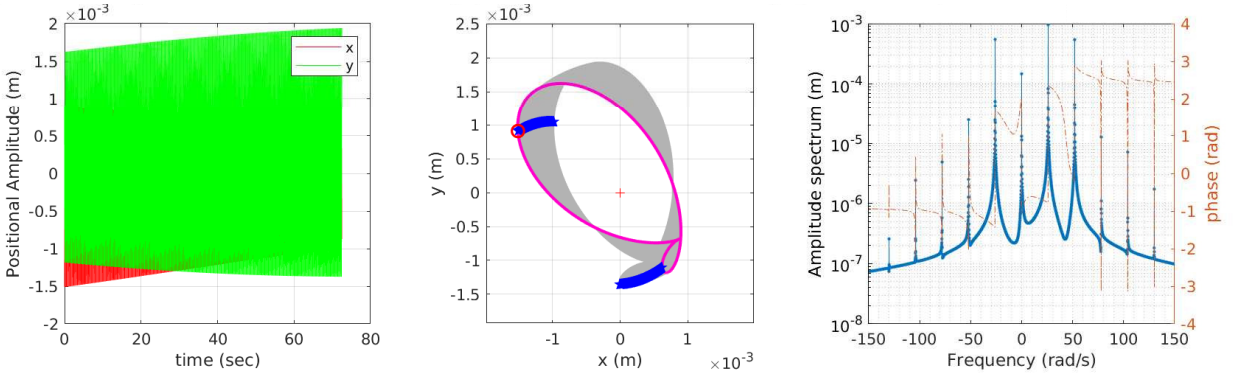

(c) $\Omega = 52.0$ rad/s, BW precessing trajectory.

Figure 22: The stagnant (period-2) orbit on the quasiperiodic $3^1{:}1^1$ branch from time simulations. In the middle column: The pink orbit shows the first quasiperiod (i.e. one repeating, precessing pattern). Blue pentagrams show the stroboscopic Poincaré section. Gray line is the trajectory of the stator that covers the time of 200 pink orbits.

The following conclusions can be drawn in this study:

On the test rig and practical aspects

1. Cubic stiffness effect can be achieved with bend-stretch coupling, despite the use of a cantilever boundary condition. Even though the cubic polynomial curve fits in both the experimental force-displacement curve and the theoretical force-displacement curve show some degree of quadratic terms, the omission of the quadratic term did not cause a large difference on the fit curve, nor on the cubic stiffness inferred.

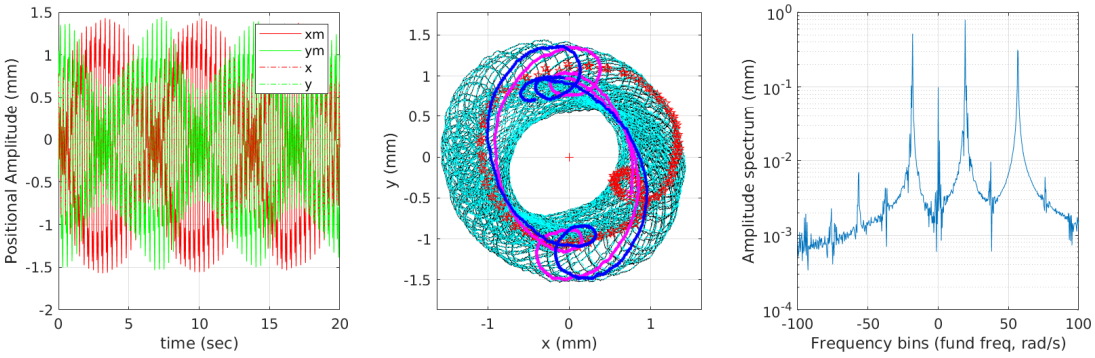

(a) Low speed orbit that is precessing FW (56.7 rad/s).

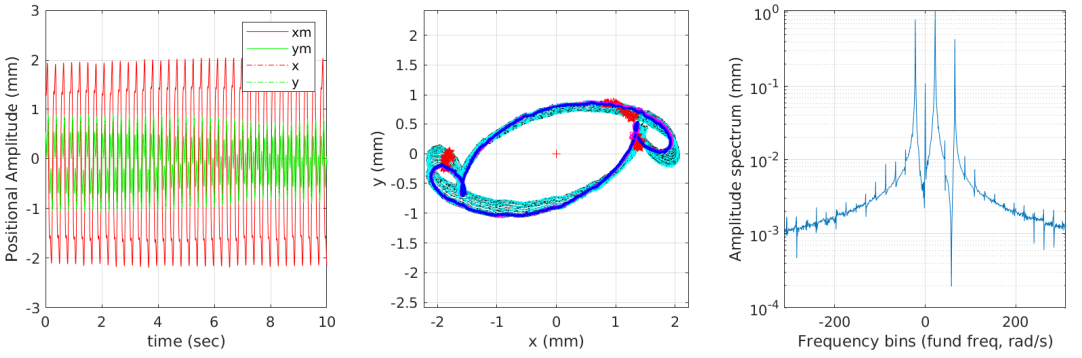

(b) The parked orbit that is not precessing (65.5 rad/s).

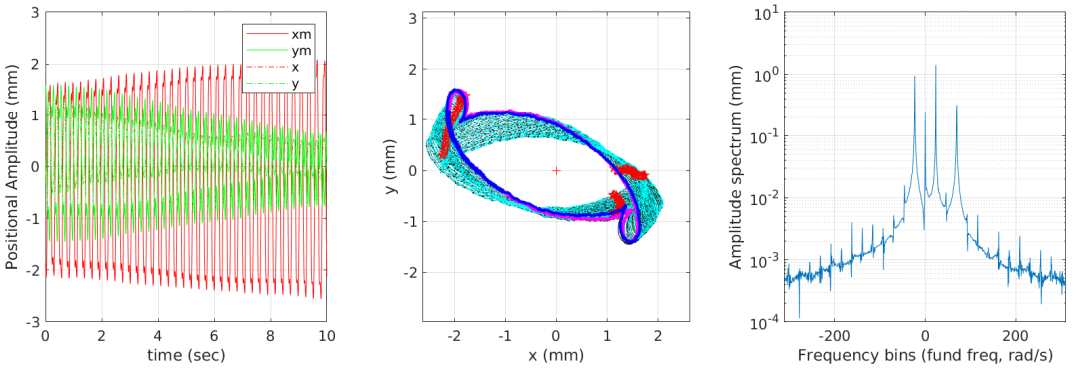

(c) The last forwards precessing orbit in the run-up direction (69.5 rad/s).

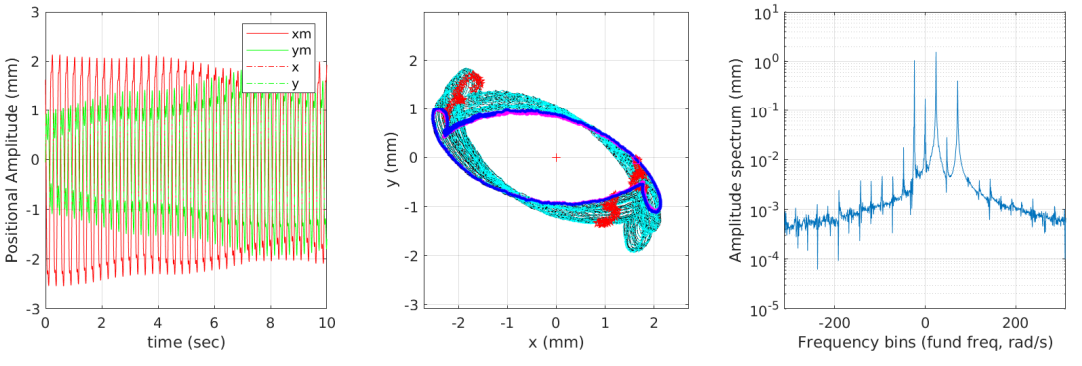

(d) The start of BW precessing orbit in the run-up direction (71.5 rad/s).

Figure 23: The parked orbit on $2^1{:}1^1$ of the experiments (see Figure 10). The first and second 1500 data points are marked pink and blue, respectively. See legend for middle figure in Table 3.

2. One of the features of the experimental design that caused complications was the use of four stiffness rods for the stator in a pinned-pinned boundary condition. Although they are tightened systematically on the stator, it was difficult to keep the stator level, resulting in uneven force carried by the rods.

3. Manufacturing difficulties included tight fitting tolerances and long thin bores. Because of the looser manufacturing tolerances than designed, excessively larger bearing fitting tolerances were adapted which resulted in slight gaps and changing support centres during the runs.

4. Modal damping obtained from the non-rotating rotor turns out to be too high in the simulations to capture the dynamics accurately, which resulted from the bearings' friction. Instead, a viscous damping coefficient that acts laterally at the stator was used effectively.

5. The protective sheets were necessary due to high unbalance forces at higher speeds, and to impact the rotor safely in order to excite various nonlinear responses.

On the observed phenomenon

1. In the experiment's numerical simulations, $2^1{:}1^1$, $3^1{:}1^1$, and $2^1{:}1^2$ IRs in the rotating frame can be predicted by the extended Campbell plots [21]. This confirms the results presented in the preceding papers [29, 55].

2. The 2:1 IR response, as well as 3:1, show sensitivity to the Campbell plot frequency line's evolution with rotor speed due to the low angles they make when intersecting.

3. In the experiments, it was observed that the rotor speeds where the nonlinear resonances were seen in the BD were consistently lower compared to the simulations. The imperfect cantilever end might have caused this effect, because when compensated via model update, the BDs can be made to overlap.

4. The main resonance was found to be bounded, contrary to the simulations where the main resonance is unbounded. The reason behind this might be the fact that the axial force on the eight 135 self-aligning ball bearings markedly increases the friction force in them. It is expected that the synchronous response is impacted the most as the almost purely circular whirl makes the response experience the high friction for longer. However, the bouncing $2^1{:}1^1$ ($2\,\omega_{f1}^{rot} = \omega_{b1}^{rot}$) resonances look unbounded, just as the simulations predict, because of a mixture of high and low amplitudes and the resulting less friction. For the sake of the structural safety of the rig, amplitudes beyond 9 mm were not excited.

5. The simulations showed the $2^1{:}1^2$ IR ($2\,\omega_{f1}^{rot} = \omega_{b2}^{rot}$) response with a small basin of attraction. They are obtained relatively easily when the damping in the simulations is decreased. However, in the experiments it was not achieved: the level of external excitation, i.e., the high angle given to the disk, was not possible even with a strong hit on the shaft and stator in opposite directions. The high level of angular momentum locked the response in the synchronous response.

6. Although the simulations did not generate self-excited backward resonance (tear-drop resonance), the experiments clearly show it. In the high unbalance case, this resonance masked the main resonance completely during the experiments. The imperfections in the support anisotropy and the bearing hub fit might have caused the elliptical orbits, which all contributed to backward whirl components around the main resonance. This, combined with the high bearing friction induced with amplitude, is responsible for the sustaining of this backward resonance that is periodic in the rotating frame.

7. In the run-up direction, for the IRs $2^1{:}1^1$ and $3^1{:}1^1$, the precession of the trajectory switched from forwards to backwards. This effect was seen in the experiments on the $2^1{:}1^1$ IR. At the transition, the orbits become *stagnant*, i.e. without any precession. Therefore, they are periodic both in the stationary frame and the rotating frame.

8. The IR trajectories pass through the space rapidly but spend more time when in a certain orientation, which was called the 'preferred' orientation. This was observed in the sustained and fully precessing, higher-speed $2^1{:}1^1$ orbits. The reason was associated with the interaction of the rotor with the slight anisotropy of the stator support.

9. The preferred orientation of the trajectory caused orbits to get *parked* in one orientation for some cases. This is in contrast to the stagnation at the switch of precession direction.

10. As in the brute force time simulations, it was very difficult to obtain the $3^1{:}1^1$ response in the experiment. Only one such response that is parked in orientation was obtained. Though, it is not clear whether this is due to the stagnation of the precession along the branch or due to the predicted reason of the anisotropy in the stator supports.

Future research ideas include control based continuation applied to nonlinear rotor-stator systems to trace the bifurcation diagrams in experiments. This would allow for analysis of the real bifurcation structure of interesting solution branches which might be difficult to model accurately with mathematical models such as the cantilever-pinned-pinned boundary conditions here. One can use actuators that are attached to the shaft with self-aligning ball bearings, in a similar way to TUD test rig [41] where this was done for damper attachment.

Funding sources

The corresponding author has received funding from the Ministry of National Education of the Republic of Türkiye which did not influence the study design, collection, analysis and interpretation of data, writing of the report or decision to submit the article for publication.

Data availability

The data is available with CC BY 4.0 license on Mendeley Data at `https://doi.org/10.17632/nv37fdydr7.1`.

Declaration of generative AI and AI-assisted technologies in the manuscript preparation process

During the preparation of this work, the authors used NotebookLM in order to extract information from various recent pieces of research. This information was then used to update the literature survey outside the AI environment. After using this tool/service, the authors reviewed and edited the content as needed and take full responsibility for the content of the published article.

Declaration of conflict of interest

The authors declare no conflict of interest.

Author contributions

The author contributions are listed as follows:

- M. S. Akay: the conception and design of the study, acquisition of data, analysis and interpretation of data, drafting the article.
- A. D. Shaw: the conception and design of the study, critical revising, supervision, final approval of the version to be submitted.
- M. I. Friswell: Supervision of the study, critical revising, final approval of the version to be submitted.

A. Displacement measurements

Displacement of the rotor system is measured by three laser sensors, two of which were Omron ZX2-LD100 and the third MTI LTC-120-40-SA tracking the position of the stator plate, labelled 'OW', 'OG' and 'MTI' respectively in Figure A.1. The use of three sensors allows detection of any angular oscillations of the stator plate about the shaft axis as follows: Figure A.1 shows the geometrical terms used to calculate lateral and angular displacements of the stator which are labelled x_s, y_s and α_s, respectively, based on the laser sensor readings. Angles β_{MTI} and β_{Omron} are included to allow for small misalignments between the frame-mounted stators and the stator. The displacements of the stator are found by,

$$y_m = y_{MTI} = x_s\left(-\frac{1}{\gamma_{MTI}}\right) + y_s\left(\frac{1}{\cos\beta_{MTI}} - \frac{\tan\beta_{MTI}}{\gamma_{MTI}}\right) + \frac{x_{MTI}}{\gamma_{MTI}} - \frac{R\tan\alpha_s/2}{\gamma_{MTI}} \tag{A.1a}$$

$$x_m = \frac{x_{OW} + x_{OG}}{2} = y_s \left(\frac{1}{\gamma_{Omron}} \right) + x_s \left(\frac{1}{\cos \beta_{Omron}} - \frac{\tan \beta_{Omron}}{\gamma_{Omron}} \right) + \frac{y_{OW} - y_{OG}}{2\gamma_{Omron}} - \frac{R \tan \alpha_s / 2}{\gamma_{Omron}} \tag{A.1b}$$

$$\tan \alpha_s = \frac{\cos \beta_{Omron}}{\frac{y_{OW}+y_{OG}}{x_{OW}-x_{OG}} - \sin \beta_{Omron}} \tag{A.1c}$$

$$\gamma_{MTI} = \cos \beta_{MTI} \cot \alpha_s + \sin \beta_{MTI} \tag{A.1d}$$

$$\gamma_{Omron} = \cos \beta_{Omron} \cot \alpha_s + \sin \beta_{Omron}. \tag{A.1e}$$

where $\beta_{Omron} = \beta_{OW} = \beta_{OG}$ is assumed for calculating x_s and y_s linearly. Displacement readings from 'OW', 'OG' and 'MTI' sensors are denoted x_{OW}, x_{OG} and y_{MTI}, respectively, and x_m and y_m are the measured values. The numerical values used are given in Table A.1. These values are measured by locating the centre of the laser point on the stator by a ruler, and visually comparing the laser beam angle to a protractor. Torsional oscillations of the stator were seen to be negligible in the vast majority of cases measured, and hence these stator measurements proved an accurate guide to the motion of the rotor system.

Table A.1
Offset values of the laser sensor setup.

Feature	Value
Stator edge size	$2R = 100.13$ mm
MTI beam offset	$x_{sh} = -0.3$ mm
OG offset	$y_A = 29.5$ mm
OW offset	$y_B = 29.5$ mm
MTI beam angle	$\beta_{sh} = -1.5$ deg
Omron beam angle	$\beta_{AB} = -0.5$ deg

B. Modified Campbell diagram

The modified values resulting in the bifurcation diagram in Figure 20b, yield the Campbell plot in Figure B.1. Note that other modifications such as on the moment of inertia values and the masses are skipped, although it would make the resulting Campbell plot overlapping that of the experimental tapping test more closely. With the modified values, the experimental Campbell plot is less overlapping. However, the cantilever end not being rigid is a fact, as well as the sensitivity of the test rig to the environment (such as the laboratory temperature). Therefore, at the moment of the data acquisition of the experiment, the Campbell plot must have been more like the one here.

CRediT authorship contribution statement

Mehmet Selim Akay: Conceptualization, Methodology, Resources, Investigation, Data Curation, Software, Formal Analysis, Validation, Visualization, Writing - Original Draft, Funding Acquisition. **Alexander D. Shaw:** Conceptualization, Methodology, Resources, Supervision, Writing - Review and Editing. **Michael I. Friswell:** Conceptualization, Supervision, Writing - Review and Editing.

References

[1] G. Jacquet-Richardet, M. Torkhani, P. Cartraud, F. Thouverez, T. Nouri Baranger, M. Herran, C. Gibert, S. Baguet, P. Almeida, L. Peletan, Rotor to stator contacts in turbomachines. Review and application, Mechanical Systems and Signal Processing 40 (2) (2013) 401–420. doi:10.1016/j.ymssp.2013.05.010.

[2] F. F. Ehrich, J. J. O'Connor, Stator whirl with rotors in bearing clearance, Journal of Engineering for Industry (1967) 381–389.

[3] H. F. Black, Interaction of a Whirling Rotor with a Vibrating Stator across a Clearance Annulus, Journal of Mechanical Engineering Science 10 (1) (1968) 1–12. doi:10.1243/jmes_jour_1968_010_003_02.

[4] S. Ahmad, Rotor casing contact phenomenon in rotor dynamics-literature survey, J. Vib. Control 16 (9) (2010) 1369–1377. doi:10.1177/107754630934160.

[5] Y. Ishida, Review of Research on Nonlinear Rotordynamics in Japan, Journal of System Design and Dynamics 7 (2) (2013) 151–169. doi:10.1299/jsdd.7.151.

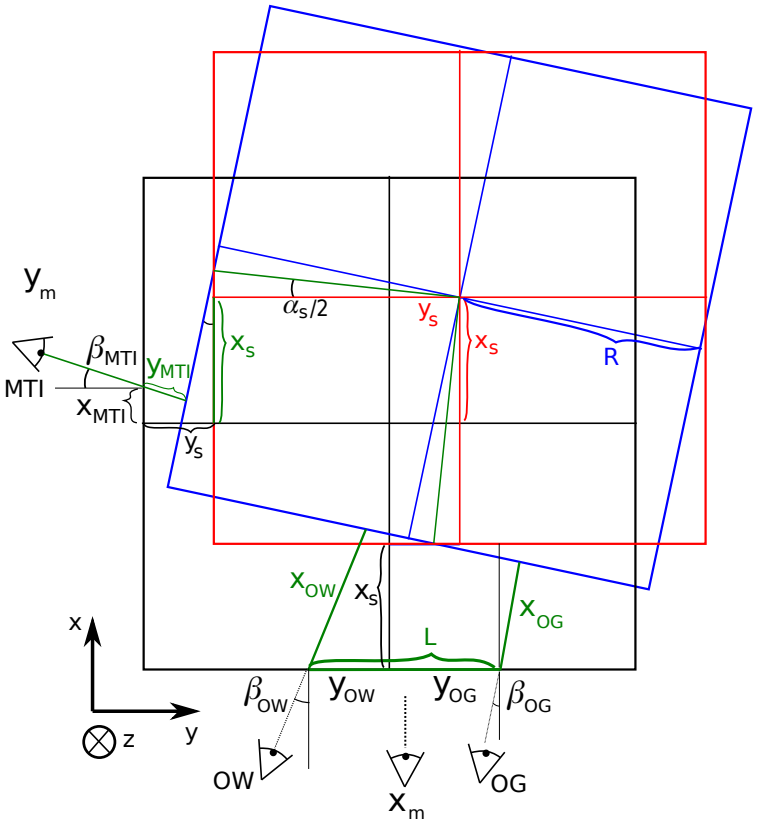

Figure A.1: Three laser sensors are used to track the stator's motion in plane (lateral displacements and the rotation angle). The stator (black), has x_s and y_s translations (red), and a rotation by angle α_s (blue). Each laser beam hits the stator (black) at an angle and an offset as indicated.

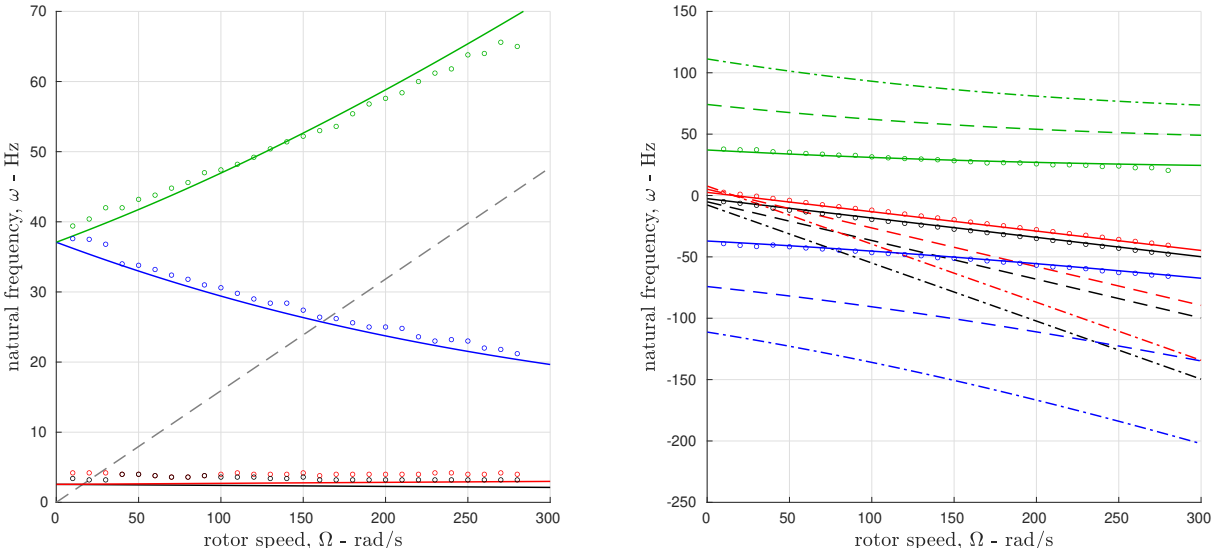

Figure B.1: Campbell diagram with the modified values: $E_1 = 270$ GPa, $k_{3b} := 0.7\,k_{3b} = 109942700$ N/m^2, and with the addition of the 7900 bearing's movement compensation as the extra shaft length $D = 65$ mm. The internal resonance speed are: 48.8 rad/s for 2^1:1^1, 32.5 rad/s for 3^1:1^1, 81.3 rad/s for 3^1:2^1, 188.3 rad/s for 2^1:1^2. (See the accompanying bifurcation diagram in Figure 20b)

[6] M. Torkhani, L. May, P. Voinis, Light, medium and heavy partial rubs during speed transients of rotating machines: Numerical simulation and experimental observation, Mechanical Systems and Signal Processing 29 (2012) 45–66. doi:10.1016/j.ymssp.2012.01.019.

[7] D. E. Bently, J. J. Yu, P. Goldman, A. Musynska, Full annular rub in mechanical seals, Part I: Experimental results, International Journal of Rotating Machinery 8 (5) (2002) 319–328. doi:10.1155/S1023621X02000301.

[8] Y. S. Choi, Investigation on the whirling motion of full annular rotor rub, Journal of Sound and Vibration 258 (1) (2002) 191–198. doi:10.1006/jsvi.5091.

[9] X. Dai, Z. Jin, X. Zhang, Dynamic Behavior of the Full Rotorstop Rubbing: Numerical Simulation and Experimental Verification, Journal of Sound and Vibration 251 (5) (2002) 807–822. doi:10.1006/jsvi.2001.3998.

[10] A. R. Bartha, Dry Friction backward whirl of rotors, Doctoral Thesis, Swiss Federal Institute of Technology (2000).

[11] M. A. Fumagalli, Modelling and measurement analysis of the contact interaction between a high speed rotor and its stator, Doctoral Thesis, Swiss Institute of Technology (1997).

[12] J. Hong, P. Yu, D. Zhang, Y. Ma, Nonlinear dynamic analysis using the complex nonlinear modes for a rotor system with an additional constraint due to rub-impact, Mechanical Systems and Signal Processing 116 (2019) 443–461. doi:10.1016/j.ymssp.2018.06.061.

[13] P. Pennacchi, N. Bachschmid, E. Tanzi, Light and short arc rubs in rotating machines: Experimental tests and modelling, Mechanical Systems and Signal Processing 23 (7) (2009) 2205–2227. doi:10.1016/j.ymssp.2009.03.008.

[14] F. Chu, W. Lu, Experimental observation of nonlinear vibrations in a rub-impact rotor system, Journal of Sound and Vibration 283 (3-5) (2005) 621–643. doi:10.1016/j.jsv.2004.05.012.

[15] Y. Ishida, M. Inagaki, R. Ejima, A. Hayashi, Nonlinear resonances and self-excited oscillations of a rotor caused by radial clearance and collision, Nonlinear Dynamics 57 (4) (2009) 593–605. doi:10.1007/s11071-009-9482-3.

[16] A. Muszynska, P. Goldman, Chaotic responses of unbalanced rotor/bearing/stator systems with looseness or rubs, Chaos Solitons Fractals 5 (9) (1995) 1683–1704. doi:10.1016/0960-0779(94)00171-L.

[17] G. A. F. Taher, E.-A. Rabeih, H. H. El-Mongy, Experimental and numerical study of lateral vibration of a rotor–stator rubbing system, International Journal of Dynamics and Control 12 (9) (2024) 3139–3154. doi:10.1007/s40435-024-01425-4.

[18] G. H. M. van der Heijden, Mode-locking in nonlinear rotordynamics, Journal of nonlinear science 5 (3) (1995) 257–283.

[19] A. Zilli, R. J. Williams, D. J. Ewins, Nonlinear Dynamics of a Simplified Model of an Overhung Rotor Subjected to Intermittent Annular Rubs, Journal of Engineering for Gas Turbines and Power 137 (6). doi:10.1115/1.4028844.

[20] A. D. Shaw, A. R. Champneys, M. I. Friswell, Asynchronous partial contact motion due to internal resonance in multiple degree-of-freedom rotordynamics, Proceedings of the Royal Society A: Mathematical, Physical and Engineering Sciences 472 (2192) (2016) 20160303. doi:10.1098/rspa.2016.0303.

[21] A. D. Shaw, A. R. Champneys, M. I. Friswell, Normal form analysis of bouncing cycles in isotropic rotor stator contact problems, International Journal of Mechanical Sciences 155 (2019) 83–97. doi:10.1016/j.ijmecsci.2019.02.035.

[22] E. T. Chipato, A. D. Shaw, M. I. Friswell, R. Sánchez Crespo, Experimental Study of Rotor-Stator Contact Cycles, Journal of Sound and Vibration 502. doi:10.1016/j.jsv.2021.116097.

[23] H. Wang, X. Shen, T. Zhou, J. Sun, G. Chen, Effects of contact stiffness on the nonlinear motions induced by impacts on an overhung rotor system, Communications in Nonlinear Science and Numerical Simulation 138 (2024) 108216. doi:10.1016/j.cnsns.2024.108216.

[24] A. Kartheek, K. Vijayan, Stochastic finite element analysis using polynomial chaos on a flexible rotor with contact nonlinearity, Nonlinear Dynamics 112 (13) (2024) 11299–11311. doi:10.1007/s11071-024-09481-3.

[25] D. Yoshimori, Y. Sugawara, M. Takeda, Bifurcation shifts in a rotor-stator contact system under frictional forces to higher rotational speeds caused by stator thickness, Mechanical Engineering Journal advpub. doi:10.1299/mej.25-00171.

[26] A. D. Shaw, M. S. Akay, M. I. Friswell, Backbone analysis for nonlinear vibrations in rotor dynamics, Nonlinear Dynamics In press. doi:10.21203/rs.3.rs-8262746/v1.

[27] E. Chipato, A. D. Shaw, M. I. Friswell, Frictional effects on the nonlinear dynamics of an overhung rotor, Communications in Nonlinear Science and Numerical Simulation 78. doi:10.1016/j.cnsns.2019.104875.

[28] R. S. Crespo, A. D. Shaw, M. I. Friswell, A. R. Champneys, Experimental characterisation of asynchronous partially contacting motion in a multiple-degree-of-freedom rotor system, Mechanical Systems and Signal Processing 145 (2020) 106904. doi:10.1016/j.ymssp.2020.106904.

[29] M. S. Akay, A. D. Shaw, M. I. Friswell, Continuation analysis of a nonlinear rotor system, Nonlinear Dynamics 105 (1) (2021) 25–43. doi:10.1007/s11071-021-06589-8.

[30] M. O. T. Cole, P. S. Keogh, Asynchronous periodic contact modes for rotor vibration within an annular clearance, Proceedings of the Institution of Mechanical Engineers, Part C: Journal of Mechanical Engineering Science 217 (10) (2003) 1101–1115. doi:10.1243/095440603322517126.

[31] C. Wang, D. Zhang, Y. Ma, Z. Liang, J. Hong, Theoretical and experimental investigation on the sudden unbalance and rub-impact in rotor system caused by blade off, Mechanical Systems and Signal Processing 76–77 (2016) 111–135. doi:10.1016/j.ymssp.2016.02.054.

[32] M. F. A. Azeez, A. F. Vakakis, Numerical and experimental analysis of a continuous overhung rotor undergoing vibro-impacts, International Journal of Non-Linear Mechanics 34 (3) (1999) 415–435. doi:10.1016/s0020-7462(98)00022-5.

[33] F. Cong, J. Chen, G. Dong, K. Huang, Experimental validation of impact energy model for the rub–impact assessment in a rotor system, Mechanical Systems and Signal Processing 25 (7) (2011) 2549–2558. doi:10.1016/j.ymssp.2011.04.004.

[34] H. Diangui, Experiment on the characteristics of torsional vibration of rotor-to-stator rub in turbomachinery, Tribology International 33 (2) (2000) 75–79. doi:10.1016/S0301-679X(00)00029-3.

[35] Y. Ishida, I. Nagasaka, T. Inoue, S. Lee, Forced oscillations of a vertical continuous rotor with geometric nonlinearity, Nonlinear Dynamics 11 (2) (1996) 107–120. doi:10.1007/BF00044997.

[36] S. Lahriri, H. I. Weber, I. F. Santos, H. Hartmann, Rotor–stator contact dynamics using a non-ideal drive—Theoretical and experimental aspects, Journal of Sound and Vibration 331 (20) (2012) 4518–4536. doi:10.1016/j.jsv.2012.05.008.

[37] I. Nagasaka, Y. Ishida, J. Liu, Forced Oscillations of a Continuous Asymmetrical Rotor With Geometric Nonlinearity (Major Critical Speed and Secondary Critical Speed), Journal of Vibration and Acoustics 130 (3). doi:10.1115/1.2890734.
[38] H. Bing, B. Chen, L. Xiang, A. Hu, K. Chen, Dynamic simulation and experimental study of dual-rotor system induced by rub-impact fault with variable state and parameter, Engineering Research Express 7 (1) (2025) 015353. doi:10.1088/2631-8695/adb373.
[39] B. Nevada, RK 4 Model Rotor Kit Datasheet - 141592 (2023).
[40] H. Yao, Y. Cao, Z. Ding, B. Wen, Using grounded nonlinear energy sinks to suppress lateral vibration in rotor systems, Mechanical Systems and Signal Processing 124 (2019) 237–253. doi:10.1016/j.ymssp.2019.01.054.
[41] U. Ehehalt, O. Alber, R. Markert, G. Wegener, Experimental observations on rotor-to-stator contact, Journal of Sound and Vibration 446 (2019) 453–467. doi:10.1016/j.jsv.2019.01.008.
[42] E. V. Karpenko, M. Wiercigroch, E. E. Pavlovskaia, R. D. Neilson, Experimental verification of Jeffcott rotor model with preloaded snubber ring, Journal of Sound and Vibration 298 (4-5) (2006) 907–917. doi:10.1016/j.jsv.2006.05.044.
[43] Y. Briend, E. Chatelet, R. Dufour, M.-A. Andrianoely, F. Legrand, G. Fiore, G. Pampolini, Nonlinear dynamics of a rotor supported by hydrodynamic bearings and ball bearings with loose fit when passing through a critical speed, Mechanical Systems and Signal Processing 210 (2024) 111146. doi:10.1016/j.ymssp.2024.111146.
[44] H. C. Piccoli, H. I. Weber, Experimental Observation of Chaotic Motion in a Rotor with Rubbing, Nonlinear Dynamics 16 (1) (1998) 55–70. doi:10.1023/A:1008284317724.
[45] C. Fu, Z. Zheng, W. Zhu, K. Lu, Y. Yang, Non-intrusive frequency response analysis of nonlinear systems with interval uncertainty: A comparative study, Chaos, Solitons & Fractals 165 (2022) 112815. doi:10.1016/j.chaos.2022.112815.
[46] Y. Qv, Z. Chang, N. Wang, T. Han, Experimental and theoretical investigation on casing vibration for dual-rotor-support-casing system with rotor-casing rub, Journal of Vibration and Control (2025) 10775463251325060doi:10.1177/10775463251325060.
[47] E. Chipato, A. D. Shaw, M. I. Friswell, Effect of gravity-induced asymmetry on the nonlinear vibration of an overhung rotor, Communications in Nonlinear Science and Numerical Simulation 62 (2018) 78–89. doi:10.1016/j.cnsns.2018.02.016.
[48] P. Varney, I. Green, Nonlinear phenomena, bifurcations, and routes to chaos in an asymmetrically supported rotor–stator contact system, Journal of Sound and Vibration 336 (2015) 207–226. doi:10.1016/j.jsv.2014.10.016.
[49] N. A. Saeed, E. M. Awwad, A. Maarouf, H. M. H. Farh, F. A. Alturki, J. Awrejcewicz, Rub-Impact Force Induces Periodic, Quasiperiodic, and Chaotic Motions of a Controlled Asymmetric Rotor System, Shock and Vibration 2021 (1) (2021) 1800022. doi:10.1155/2021/1800022.
[50] S. W. Shaw, Chaotic dynamics of a slender beam rotating about its longitudinal axis, Journal of Sound and Vibration 124 (2) (1988) 329–343. doi:10.1016/S0022-460X(88)80191-3.
[51] Y. Cao, H. Yao, Q. Li, P. Yang, B. Wen, Vibration mitigation and dynamics of a rotor-blade system with an attached nonlinear energy sink, International Journal of Non-Linear Mechanics 127. doi:10.1016/j.ijnonlinmec.2020.103614.
[52] K. Mora, A. R. Champneys, A. D. Shaw, M. I. Friswell, Explanation of the onset of bouncing cycles in isotropic rotor dynamics; a grazing bifurcation analysis, Proceedings of the Royal Society A: Mathematical, Physical and Engineering Sciences 476 (2237) (2020) 20190549. doi:10.1098/rspa.2019.0549.
[53] E. V. Karpenko, M. Wiercigroch, E. E. Pavlovskaia, M. P. Cartmell, Piecewise approximate analytical solutions for a Jeffcott rotor with a snubber ring, International Journal of Mechanical Sciences 44 (3) (2002) 475–488. doi:10.1016/S0020-7403(01)00108-4.
[54] E. T. Chipato, A. D. Shaw, M. I. Friswell, Nonlinear rotordynamics of a MDOF rotor–stator contact system subjected to frictional and gravitational effects, Mechanical Systems and Signal Processing 159. doi:10.1016/j.ymssp.2021.107776.
[55] M. S. Akay, A. D. Shaw, M. I. Friswell, Continuation analysis of overhung rotor bouncing cycles with smooth and contact nonlinearities, International Journal of Non-Linear Mechanics 150 (2023) 104343. doi:10.1016/j.ijnonlinmec.2022.104343.
[56] M. S. Akay, Nonlinear Interactions in Rotordynamics: Numerical and Experimental Investigations of Internal Resonances, Ph.D. thesis, Swansea University, UK (Oct. 2025).
[57] M. I. Friswell, J. E. T. Penny, S. D. Garvey, A. W. Lees, Dynamics of Rotating Machines, Cambridge University Press, 2010.
[58] T. Inoue, Y. Ishida, Chaotic vibrations and internal resonance phenomena in rotor systems, Journal of vibration and acoustics 128 (2) (2006) 156–169. doi:10.1115/1.2149395.